Structural Determination of Ordered Porous Solids by Electron Crystallography

*Tom Willhammar, Yifeng Yun, and Xiaodong Zou**

Knowing the structure of porous materials is essential for understanding their properties and exploiting them for applications. Electron crystallography has two main advantages compared to X-ray diffraction for structure determination. Crystals too small or too complicated to be studied by X-ray diffraction can be studied by electron crystallography. The crystallographic structure factor phase information, which is lost in X-ray diffraction, can be obtained from high-resolution transmission electron microscopy (HRTEM) images. Here, different electron microscopic techniques and their applications for structure determination of porous materials are reviewed. The recently developed automated diffraction tomography (ADT), the rotation electron diffraction (RED), and the through-focus structure projection reconstruction (QFcous) methods make the structure determination by electron crystallography more feasible for non-TEM experts and as efficient as that by X-ray diffraction. How the various electron crystallographic methods are chosen are demonstrated and these methods used for solving different structural problems in porous materials. The benefits of combining electron crystallography and X-ray diffraction for studying complex zeolite structures are also shown. A large number of examples are given to demonstrate the use of various electron crystallographic techniques for structure determination of zeolites, metal-organic frameworks and ordered mesoporous materials. These electron crystallographic methods are general and can also be used for structural studies of other functional materials.

1. Introduction

Ordered porous solids have narrow pore size distributions, well-defined pore shapes and channel systems, and large surface areas. They have attracted wide interests because of their industrial applications in catalysis, ion-exchange, sorption and separation.[1] The knowledge about the structures of porous solids is essential for understanding their properties, for developing new applications and for designing new porous materials. Porous solids can be classified according to their pore size: microporous materials for those with the pore sizes equal or below 2 nm, mesoporous materials for those with the pore sizes between 2 nm and 50 nm, and macropores for those with the pore sizes above 50 nm. They can also be classified according to the solid composition: inorganic materials such as zeolites,[2] open-framework oxide[3] and mesoporous silica,[4] inorganic and organic hybrids such as metal–organic frameworks (MOFs)[5] and organic frameworks for example covalent organic frameworks (COFs).[6] Structure determination of these porous materials is often challenging because many porous materials are often polycrystalline, their structures are often complex with large unit cells, and the materials are sometimes disordered. The most common techniques used for structure determination of porous solids are single crystal X-ray diffraction (SXRD), powder X-ray diffraction (PXRD) and transmission electron microscopy (TEM).

The most feasible and mature technique for structure determination is single crystal X-ray diffraction. Complete three-dimensional X-ray diffraction intensity data can be obtained from a single crystal in less than 10 h on an in-house diffractometer and less than an hour using a synchrotron light source. The intensities from SXRD are kinematical and have been used to solve unknown structures of a large variety of complexity. In most cases, the structure solution is straight-forward and can be done in a few hours. The major limitation of structure determination by SXRD is the crystal size, which needs to be at least a few micrometers even using a brightest synchrotron light source. Another limitation is that it is difficult to determine structures of disordered crystals by SXRD. Single crystal X-ray diffraction has been used for structure determination of numerous open-framework oxides[7] and metal-organic frameworks[5] because it is relatively easy to obtain large-enough single crystals of such materials. On the contrary, only limited number of zeolite materials was synthesized as single crystals. During the past five years, eleven new zeolite framework structures have been solved by single crystal X-ray diffraction. These are aluminogermanates (PKU-9 (PUN)),[8] silicogermanates (SU-15 (SOF), SU-32 (STW)),[9] gallogermanates (CJ63 (JST), JU-64 (JSR)),[10,11] aluminophosphates (CJ40 (JRY), CJ62 (JSW), CJ69 (JSN)),[10,12] the beryllosilicate LSJ-10 (JOZ)[13] and the high silica zeolite SSZ-57 (*SFV) with a disordered modulated structure.[14]

While open-framework metal oxides, germanate- and phosphate-based zeolites and metal-organic frameworks can form

T. Willhammar, Y. F. Yun, Prof. X. D. Zou
Berzelii Center EXSELENT on Porous Materials
Department of Materials and Environmental Chemistry
Stockholm University
SE-106 91, Stockholm, Sweden
E-mail: xzou@mmk.su.se

DOI: 10.1002/adfm.201301949

crystals large enough for single crystal X-ray diffraction, other materials such as silicate-based zeolites and covalent organic frameworks are often synthesized as polycrystalline materials, too small to be studied by SXRD. In such cases, powder X-ray diffraction has been an obvious choice. PXRD data is collected from millions of randomly oriented crystals so that strong enough diffraction intensities can be obtained. The data collection is very simple and takes less than an hour. However, because intensities from differently oriented crystals are measured simultaneously, reflections with similar *d*-spacings will overlap in the powder diffraction pattern. The intensity of each reflection cannot be determined unambiguously, which makes the structure determination by PXRD much more difficult than that by SXRD. Reflection intensities are extracted from PXRD data after a Le Bail fitting, which can give approximate single-crystal-like data for structure solution. Different methods have been developed to deal with the overlap problem and to solve unknown structures by PXRD data.[15] During the past eight years, PXRD has been the most important technique for structure determination of zeolites. More than 15 new zeolite structures have been solved from PXRD data. These are the ITQ-series (ITQ-32, ITQ-33 (ITT), ITQ-34 (ITR), ITQ-44 (IRR), ITQ-49),[16] SSZ-series (SSZ-52 (SFW), SSZ-56 (SFS), SSZ-65 (SSF), SSZ-77 (SVV) and SSZ-82(SEW)),[17] IM-series (IM-16 (UOS) and IM-20 (UWY)),[18] LZ-135 (LTF),[19] STA-15 (SAF),[20] MCM-70 (MVY),[21] Linde type J (LTJ),[22] COK-14 (OKO)[23] and the oxonitridophosphate-2 (NPT).[24] Recently we demonstrated that zeolites and open-framework structures could be solved from PXRD data using a direct-space structure solution algorithm based on the building units identified by for example infrared spectroscopy.[25]

Although structure solution by powder diffraction has been more and more powerful, structures of many porous materials can still not be solved by PXRD alone. These include complex structures with large unit cells that cause severe reflection overlapping, and/or crystals containing defects such as intergrowth and stacking disorders. PXRD patterns of mesoporous silica and covalent organic frameworks are often very poor and contain very few and broad diffraction peaks. For such materials, electron crystallography is the best alternative.

Electron crystallography is an important tool for structure determination of materials where the crystals are too small to be studied by SXRD or the structures too complex to be studied by PXRD. One important advantage of using electrons instead of X-rays is that electrons interact with matter much stronger than do X-rays and can be used for studying nano-sized crystals. This means that X-ray powder samples behave like single crystals under the electron beam. Another unique advantage is that electrons are negatively charged and can be focused by electromagnetic lenses to form images. High resolution transmission electron microscopy (HRTEM) images can provide detailed information about atomic arrangements in a crystal and possible disorders can be directly seen by HRTEM. Electron crystallography has become more and more important for structure determination of unknown zeolites. Since 2006, 12 novel zeolite structures have been solved by electron crystallography alone or in combination with other techniques. These are TNU-9 (TUN),[26] IM-5 (IMF),[27] SSZ-74 (-SVR),[28] ITQ-26 (IWS),[29] ITQ-37 (-ITV),[30] ITQ-38,[31] ITQ-39,[32] ITQ-40,[33] ITQ-43,[34] ITQ-51 (IFO)[35] and SU-78.[36] Electron crystallography has also been used for studying metal-organic frameworks, and pore structures and pore dimensions in ordered mesoporous materials. The power of electron microscopy for structure analysis of porous materials has been reviewed in several articles.[37]

In this review we present the different electron crystallographic techniques and their applications on structure determination of porous materials. We will describe several advanced

Tom Willhammar is a PhD student in Structural Chemistry at the Department of Materials and Environmental Chemistry, Stockholm University. He received his Master's Degree in Chemical Engineering from Lund University in 2008. His main research interest is electron crystallography and porous materials, particularly applying electron microscopy imaging to structural studies of zeolites.

Yifeng Yun is a PhD student in Inorganic Chemistry under Prof. Xiaodong Zou at the Department of Materials and Environmental Chemistry, Stockholm University. He received his BSc in Chemical Engineering and Technology in 2008 at the Central South University, China. He then spent two years in Master's studies in analytical chemistry at the same university. He mainly works on structure solutions of crystalline materials by electron crystallography.

Xiaodong Zou is the chair of Inorganic and Structural Chemistry and Deputy Head of the Department of Materials and Environmental Chemistry, Stockholm University. She received her BSc in physics from Peking University (1984) and her PhD in structural chemistry from Stockholm University (1995). Her research interests include method development and the application of electron crystallography for structure determination of nanosized materials, and the synthesis and applications of zeolites, inorganic open-framework materials, and metal–organic frameworks.

methods that are important for structure determination by electron crystallography: Precession electron diffraction (PED),[38] 3D electron diffraction tomography as represented by automated diffraction tomography (ADT)[39] and rotation electron diffraction (RED),[40] structure projection reconstruction by image processing,[41–43] and three-dimensional reconstruction from HRTEM images.[44] The recently developed techniques have made the structure determination by electron crystallography more feasible, even for non-TEM experts. We will demonstrate how the various electron crystallographic methods are chosen and used for solving different structural problems in porous materials. We will also show the benefits of combining electron crystallography and X-ray diffraction for studying complex zeolite structures. We give a large number of examples where various electron crystallographic techniques are used and combined for structure determination of zeolites, metal-organic frameworks and ordered mesoporous materials.

2. Advanced Electron Crystallographic Methods

Both electron diffraction and HRTEM can be used for structure determination of porous materials. The advantage of using HRTEM images is that both the structure factor amplitudes and phases, which are needed for structure determination, can be obtained directly from HRTEM images. In diffraction, the structure factor phase information is lost and has to be determined by other methods. On the other hand, it is relatively easier to collect good electron diffraction patterns than to take high quality HRTEM images.

2.1. Precession Electron Diffraction and 3D Electron Diffraction Tomography Techniques

The first publication of structure determination by electron diffraction (ED) was reported already in 1937.[45] Although methods for quantifying electron diffraction patterns are developed[46] and examples of structure solution by electron diffraction were reported,[47,48] the development of this method was hampered by the fear of dynamical effects. It was difficult to obtain complete 3D electron diffraction data because one needs to collect a large number of individual ED patterns along different zone axes. Furthermore, it was not easy to merge the 2D ED data into the 3D data. Structure determination by electron diffraction has been time consuming and required extensive expertise.

The recent developments on new electron diffraction techniques have made structure determination by electron diffraction more feasible. The precession electron diffraction (PED) technique invented by Vincent and Midgley in 1994[38] brought large attentions and interests in using the electron diffraction data for structure solution. The electron precession is often controlled by dedicated PED hardware; the incident electron beam is tilted away by an angle from the optical axis and precessed around the optical axis. The PED pattern is an integration of all ED frames during the beam precession. We recently developed a software-based method for collecting PED data,[49] where individual ED frames before the combination are collected and saved. The ED frames can be combined later to generate the PED pattern. Compared to conventional electron diffraction, the resolution of PED is higher and dynamical effects are reduced, due to the off-axis beam inclination where fewer reflections are excited simultaneously at the exact Bragg condition.[50] Precession electron diffraction has been used for solving unknown structures of inorganic compounds[51] and zeolites.[52] Intensities were extracted from PED patterns along different zone axes and merged to obtain 3D PED data for the structure solution.

Recently two automated methods have been developed for complete 3D electron diffraction data collection and processing: automated diffraction tomography (ADT)[39] and rotation electron diffraction (RED).[40] In both ADT and RED methods, electron diffraction frames can be collected in either selected area electron diffraction (SAED) mode or nano-electron diffraction (NED) mode. The ADT method is performed on a scanning transmission electron microscope (STEM) with or without precession. ED frames are collected sequentially in a fine step (usually 1°) by tilting around an arbitrary axis of a crystal. The sequential crystal tilt is computer-controlled and crystal tracking during the tilt can be done in TEM or STEM mode. The software package ADT3D was developed for processing the ED frames and extracting the ED intensities, which includes the reconstruction of reciprocal space, determination of the unit cell parameters, reflection indexation and intensity integration.

The rotation electron diffraction (RED) method runs in the TEM mode. The RED data collection combines the goniometer tilt with a fine electron beam tilt, which allows the collection of 3D electron diffraction data with fine sampling steps down to 0.001°.[40] The data collection is controlled by the RED data collection software package.[40] Typically a beam tilt of 0.1–0.4° per step is combined with a goniometer tilt of 2–3° around a common tilt axis. More than 1000 ED frames can be collected in less than one hour using this method. The ED patterns are analyzed using the RED data processing software package,[40] which includes shift correction, peak search, unit cell determination, indexation of reflections, and intensity extraction.

The 3D ADT and RED methods have many advantages compared to the conventional 2D zone-axis electron diffraction methods. Firstly almost complete 3D data can be collected from one single crystal; the data within the missing cone may be generated from the symmetry-related reflections or collected from another crystal with different orientations. Secondly dynamical effects can be reduced because fewer reflections are present in each ED frame compared to a zone-axis ED pattern. More importantly, there is no need to have a crystal zone axis aligned in parallel to the electron beam and the data collection can start from any arbitrary orientation of the crystal. This means that the data collection no longer requires skilled operators and is feasible for non-TEM experts. The development of the ADT and RED methods has been revolutionary and turned a transmission electron microscope into a single crystal electron diffractometer. Complete 3D single crystal ED data can be collected from crystals of 50 nm in size, millions times smaller than what is needed on a synchrotron source. As it will be shown later, the ADT and RED intensities have good quality and can be used for ab initio structure solution and refinement. A large and rapidly increasing number of new structures have been

solved from the 3D electron diffraction data, among which are several zeolites and metal-organic frameworks.

2.2. High-Resolution Transmission Electron Microscopy and Structure Projection Reconstruction by Image Processing

HRTEM is the most common imaging technique used for studying porous materials at atomic scale.[44] Recent developments of transmission electron microscopes with image aberration correctors have pushed the resolution limit into the sub-Ångström level. However, for porous materials such as zeolites, metal-organic frameworks and mesoporous materials, the image resolution is mainly limited by the materials due to the electron beam damage and not by the TEM. The stability of a porous material under electron beam can vary greatly, depending on the structure and composition of the material, and the guest species in the pores.

Taking good HRTEM images of porous materials is very challenging. Low electron-doses are often needed in order to minimize the radiation damage, and thus the signal to noise ratio in the obtained HRTEM images is usually very low. Working under low electron-dose conditions requires high TEM skills and patience. More seriously, HRTEM image are usually not directly interpretable in terms of structure projection due to various reasons. One reason is the dynamical effects that electrons are scattered more than once when passing through the sample. This should be minimized by working on very thin crystals. Another reason is the optical distortions caused by lens aberrations in the TEM. The image contrast changes with the imaging conditions, for example the alignment of the electron optics and the focus of the objective lens, see **Figure 1**a–d.

The HRTEM images show very different contrasts and do not always represent the structure projection (Figure 1a–d). At different defocus values, the objective lens of a TEM transfers the structure to an HRTEM image differently, changing the contrast of the image. The effects of defocus and other optical parameters on an HRTEM image can be represented by a contrast transfer function (CTF) $T(\mathbf{u})$:[50]

$$T(\mathrm{u}) = D(\mathrm{u})\sin\chi(\mathrm{u}) = D(\mathrm{u})\sin(\pi\varepsilon\lambda\mathrm{u}^2 + {}^1/_2\pi C_s\lambda^3\mathrm{u}^4) \quad (1)$$

where λ is the electron wavelength, ε the defocus value and C_s the spherical-aberration coefficient of the objective lens. $D(\mathbf{u})$ is an envelope function that slowly decreases from one at $u = 0$ to zero at $u =$ infinitive due to the partial coherence of the electron beam. Once the defocus value is determined, the CTF can be calculated according to Equation (1).

The CTF transfers the diffracted electron beams in different ways. The diffraction amplitudes are directly proportional to the structure factors $F(\mathbf{u})$ of the crystal under kinematical approximation. The structure factors $F(\mathbf{u})$ is defined as

$$\mathrm{F(u)} = \sum_{\mathrm{j}=1}^{\mathrm{N}} \mathrm{f_j(u)} \exp 2\pi i(\mathrm{u}\cdot\mathrm{r_j}) \quad (2)$$

where $\mathrm{f_j}(\mathbf{u})$ is the atomic scattering factor of the $\mathrm{j^{th}}$ atom in the unit cell and N is the total number of atoms. $F(\mathbf{u})$ is a complex and contains an amplitude part $|F(\mathbf{u})|$ and a phase part $\phi(\mathbf{u})$

$$F(\mathrm{u}) = |F(\mathrm{u})|\exp[i\phi(\mathrm{u})] \quad (3)$$

For thin crystals, the HRTEM image is related to the crystal projection in a simple way, and the crystallographic structure factors $F(\mathbf{u})$ can be obtained from the HRTEM image by

$$F(\mathrm{u}) = \frac{I(\mathrm{u})}{kT(\mathrm{u})} \ (\mathrm{for}\, T(\mathrm{u}) \neq 0) \quad (4)$$

where $I(\mathbf{u})$ is the Fourier transform of the image and k is a constant. Equation (4) shows that the phases of $F(\mathbf{u})$ and $I(\mathbf{u})$ are the same if $T(\mathbf{u}) > 0$ and differ by 180° if $T(\mathbf{u}) < 0$.[44] An HRTEM image can be interpreted directly in terms of the structure projection only if it is taken under the optimum defocus conditions (i.e. near the Scherzer defocus) at which $F(\mathbf{u})$ and $I(\mathbf{u})$ have the same phases (Figure 1b). For HRTEM images taken under other conditions, different image processing approaches can be used for retrieve the structure projection.

One approach to reconstruct structure images is crystallographic image processing of HRTEM images.[41,42] The defocus and astigmatism values can be determined from the Fourier transform of the HRTEM image, if there exists amorphous region on the crystal. The effects of the CTF on the HRTEM image can be compensated for by image processing, according to Equation (1) and (4). This image can be further improved by imposing the crystallographic symmetry. These procedures can

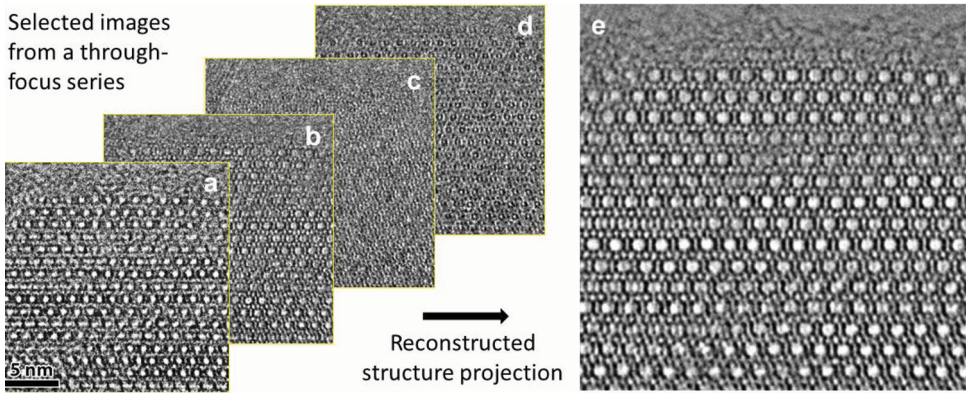

Figure 1. (a–d) HRTEM images of zeolite ITQ-39 taken along [100] from the same crystal area but with different defocus values,[32] (a) –678 Å, (b) –358 Å, (c) -38 Å and (d) +282 Å. (e) A structure projection image reconstructed from 20 HRTEM images. The defocus determination and structure projection reconstruction were carried out using the program QFocus.[43] Reprinted with permission.[32] Copyright 2012, Macmillan Publishers Ltd.

be carried out by the crystallographic image processing software CRISP[41] and works for single HRTEM images.[53] Crystallographic image processing is especially helpful for HRTEM images of periodic objects with low signal to noise ratios, where the image quality can be improved by averaging the unit cells and imposing the symmetry.

For crystals where the periodicity is interrupted by faults and boundaries, unit cell averaging and symmetry cannot be applied. If there is little amorphous region in the HRTEM image, it is difficult to determine the defocus and astigmatism from a single image. Recently we have developed a structure projection reconstruction method from through-focus series of HRTEM images.[43] The defocus values are determined jointly from the through-focus series of HRTEM images with a known defocus step by evaluating the phase similarities of $F(\mathbf{u})$ over the entire u-values (pixels) in the Fourier transforms of the HRTEM images. $F(\mathbf{u})$ is calculated according to Equation (4) using a trial defocus value for the first image in the series. The defocus values for other images are calculated from the trial defocus value and the defocus step. The trial defocus value with the highest phase similarity will be the correct defocus. The two-fold astigmatism in the HRTEM images can also be estimated. A projected electrostatic potential image is obtained from each HRTEM image in the series by the CTF correction based on Equation (1) and (4) using to the following equation:

$$\phi(\mathrm{r}) = k \sum_{\mathrm{u}} F(\mathrm{u}) \exp[-2\pi i(\mathrm{u}\cdot\mathrm{r})] = \sum_{\mathrm{u}} \frac{I(\mathrm{u})}{T(\mathrm{u})} \exp[-2\pi i(\mathrm{u}\cdot\mathrm{r})] \tag{5}$$

The final corrected images were added together to reconstructed an image that is closer to the structure projection than the individual images (Figure 1e). The structure projection reconstruction method has been implemented into the computer program QFocus.[43] The number of HRTEM images in a through-focus series is typically 10–20.

The through-focus structure projection reconstruction method using the program QFocus is more general and can be applied to both periodic and non-periodic objects. This is especially useful on beam-sensitive and disordered materials, because the signal to noise ratio can be greatly enhanced by averaging reconstructed images taken at different defocus values. It is also beneficial for non-TEM experts and save time, because there is no need in finding the optimum defocus value when recording an HRTEM image, which also avoids unnecessary exposure of the sample to electrons. The chance to obtain a good structure image after image processing is greatly increased. The structure image can be used to build structure model and determine the crystallographic structure factors, which are important for structure determination. The later can be done using the crystallographic image processing program CRISP.[41,42,44,53]

2.3. 3D Reconstruction of HRTEM Images

Because each HRTEM image is only a 2D projection of a 3D structure, it is necessary to combine images from different projections to reconstruct the 3D structure. The 3D reconstruction is performed in reciprocal space by determining the crystallographic structure factor F(hkl) from a series of projections. The 3D electrostatic potential distribution $\phi(xyz)$ inside a crystal can be calculated from the structure factors F(hkl) by inverse Fourier transformation:

$$\phi(xyz) = \frac{\lambda}{\sigma\,\Omega} \sum_{hkl} \mathrm{F}(hkl) \exp[-2\pi i(hx + ky + lz)] \tag{6}$$

where σ the interaction constant and Ω the unit cell volume.

A 3D electrostatic potential map can be obtained by Fourier summation of structure factors for all reflections using Equation 6. If the resolution is high enough so that peaks in the reconstructed 3D electrostatic potential map are well-resolved, the atomic positions can be directly located from the 3D map. The resolution that is needed to resolve the desired atoms should be higher than the interatomic distances, for example 1.6 Å for Si–O and 3.1 Å for Si–Si distances. For zeolites, it is often sufficient to find the Si/Al positions in order to build a framework model, since oxygen atoms are always located between the Si/Al atoms. Light atoms are always difficult to be seen in the presence of heavy elements. For metal-organic frameworks, it is often enough to find the positions of metal clusters to construct the structure model, since the structure of the organic linker is well-defined.

Theoretically, one might expect that it is necessary to collect all reflections within a desired resolution range in order to obtain the 3D potential map from which atomic positions are determined. However, it is very time-consuming and practically impossible to collect all the projections. The number of projections that is needed for a 3D structure determination depends on the symmetry of the crystal and how the strong reflections are distributed. It is enough to determine the structure factors of symmetry-independent reflections, other reflections can be generated according to the symmetry.[44] The higher the symmetry, the fewer number of projections must be measured. **Figure 2** illustrates the significance of strong and weak reflections, phases and amplitudes on a structure solution. It can be seen that strong reflections are more important than weak reflections for structure solution, because strong reflections contribute more to the potential in a 3D potential map than weak reflections. Missing strong reflections may result in a wrong 3D map. In fact, weak reflections can be ignored during structure solution, but they are important for the structure refinement. Furthermore, structure factor phases are more important than amplitudes, because they determine the locations of the peak maxima and thus the atomic positions. Amplitudes, on the other hand, mainly affect the relative peak heights.

In conclusion, in order to obtain a 3D electrostatic potential map from which the most significant (heavy) atomic positions can be located, we need to collect all strong reflections within the asymmetric unit, and be sure that the phases of the strongest reflections are correctly determined. A number of complex structures have been solved by 3D reconstruction from HRTEM images, including oxides, intermetallic phases, mesoporous silica and zeolites. This method is rather demanding and often requires extensive experimental work by well-trained electron microscopists to take good HRTEM images. One example is the structure solution of the quasicrystal approximant υ-AlCrFe, where HRTEM images from 13 zone axes were used for the 3D reconstruction.[54] It is one of the most complex inorganic structures solved by electron crystallography, with 129

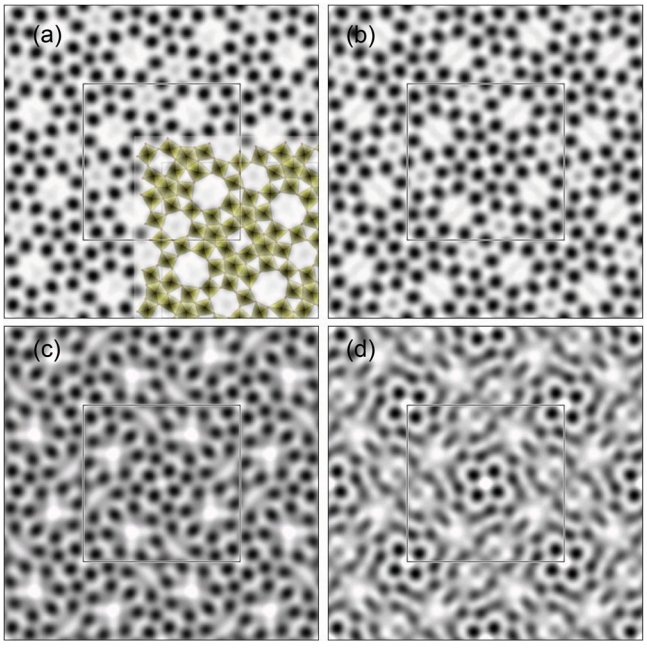

Figure 2. Significance of strong and weak reflections, phases and amplitudes for the structure solution, demonstrated here using the potential map of $K_2O{\cdot}7Nb_2O_5$ projected along the *c*-axis. (a) Projected electrostatic potential map reconstructed from an HRTEM image. Insert: the structure model. All Nb atoms are resolved. The positions of oxygen atoms are between the Nb atoms. (b) A map using only the strongest half of the reflections. The map is very similar to that in (a), showing that the weak reflections are less important for structure solution. (c) A map with all amplitudes set equal and phases unchanged from those used in (a). The Nb peaks are sharp and clearly resolved. This shows that as long as the phases are correct, the amplitudes can have large errors in structure solution. (d) A map with the phase of one strongest reflection shifted by 180° while all other amplitudes and phases are kept the same as in (a). The map now differs significantly from (a). The peaks are no longer sharp and some have shifted from those seen in (a). This shows that for a correct structure solution, the phases of the strongest reflections must be correct.

symmetry-independent atoms. A simpler and more feasible approach for structure determination of complex structures is to combine electron crystallography and powder X-ray diffraction. This is especially useful when the number of structure factor amplitudes and phases obtained from the HRTEM images are not enough or the quality is high enough to reach the structure solution. The structure factor phases obtained from the HRTEM images can be used as initial phases for structure determination by PXRD. The combination of electron crystallography and powder X-ray diffraction has been essential for the structure solution of three most complex zeolite structures.[26–28]

3. Structure Determination of Zeolites by Electron Diffraction

3.1. Structure Determination of Zeolites by Combining Zone Axis ED Patterns

Conventional selected-area electron diffraction (SAED) and precession electron diffraction (PED) patterns are often taken along a certain crystal direction (called zone axis) and the patterns appear symmetrical (**Figure 3**a–c). ED patterns from different zone axes can be collected from one or several crystals. Many zeolite structures such as MCM-22,[46] SSZ-48,[55] ITQ-40[33] and ZSM-10[56] have been solved by SAED.

SSZ-48 is a large-pore high-silica zeolite synthesized using *N,N*-diethyl-decahydroquinolinium as the organic structure directing agent (OSDA). It was the first unknown zeolite material solved by electron diffraction (Figure 3). SAED patterns from 11 zone axes were collected from needle-like crystals of ca. 0.05 μm × 0.25 μm × 10 μm in size. Integrated ED intensities were extracted from SAED patterns and merged together to generate 326 symmetry-independent reflections (d < 0.99 Å). The space group ($P2_1$) and the unit cell parameters (a = 11.19 Å, b = 4.99 Å, c = 13.65 Å and β = 100.7°) were deduced from the 3D electron diffraction data. The ED intensities were used for the structure solution of SSZ-48 by direct methods. All seven silicon positions, five of the 14 oxygen positions and 9 carbon positions from the SDA could be located. The remaining oxygen atoms were positioned between the Si atoms and refined using distance-least-squares refinement. The final structure was refined against high-resolution synchrotron powder X-ray diffraction.[55] Many examples of structure determination of zeolites using SAED data were reported by Dorset et al.[57]

ITQ-40 is an extra-large pore germanosilicate synthesized using diethyldiphenylphosphonium (Et_2Ph_2POH) as the OSDA.[33] The space group ($P6_3/mmc$) and the unit cell parameters (a = 16.42(10) Å, c = 31.90(8) Å) were determined by SAED. Intensities of 98 reflections were extracted from SAED patterns taken along the [001] and [100] zone axes. The structure was solved from the SAED data using maximum entropy and likelihood via the computer program MICE.[58] The structure of ITQ-40 contains both double four-rings and double three-rings and has 15-ring channels along the *c*-axis and 16-ring channels perpendicular to the *c*-axis. ITQ-40 has one of the lowest framework densities among all zeolites (10.1 T-atoms/1000 Å^3). The structure was later also solved by powder X-ray diffraction and single crystal X-ray diffraction.

Precession electron diffraction can reduce significantly dynamical effects and secondary scattering in electron diffraction.[49–51] Dorset et al. compared structure determination of various zeolites by PED with that by SAED, and showed that PED data can be used for ab initio structure determination of zeolites.[52] The maximum entropy and likelihood phasing method has shown to be powerful in phasing both the SAED and PED data and solving the zeolite structures.[52]

Dorset et al. also used PED patterns to confirm the space group ($P6/mmm$) and unit cell parameters (a = 31.475 Å, c = 7.551 Å) of the aluminosilicate ZSM-10 and to distinguish two models proposed in 1996 by Higgins and Schmitt.[56] The final model was refined against the PXRD data. ZSM-10 is built of stacked cancrinite cages and hexagonal prisms.

Structure determination using zone-axis SAED or PED patterns are not straightforward. The crystals have to be aligned manually along the individual zone axes. The new 3D electron diffraction tomography techniques ADT and RED have made a breakthrough for the structure determination using ED data. The automated 3D ED data collection combined with the fast

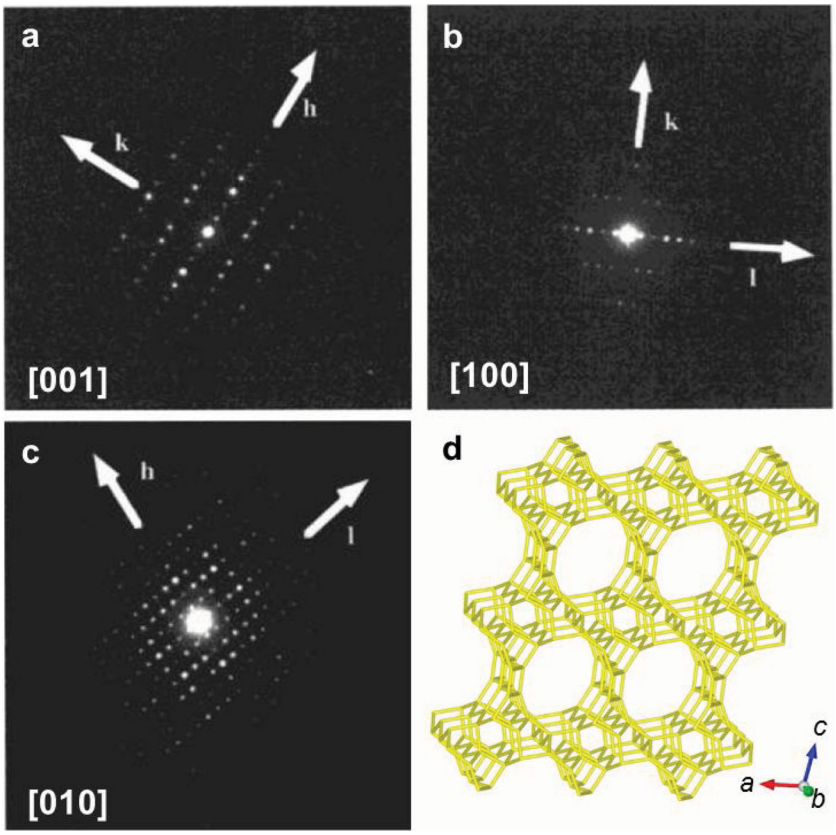

Figure 3. Electron diffraction data from three main zone axes of SSZ-48 and the corresponding model obtained from electron diffraction by direct methods. Adapted with permission.[55] Copyright 1999, American Chemical Society.

data processing procedures makes the structure determination from electron diffraction as feasible as that by single crystal X-ray diffraction, but from crystals millions times smaller.

3.2. Structure Determination of Zeolites by Combining ED and PXRD

Electron diffraction has been combined with PXRD for structure determination of zeolites. Different strategies have been applied to combine the ED and PXRD data. One strategy is to retrieve the structure factor phases from the ED data. The obtained structure factor phases can be used as the initial phases for the structure solution using PXRD data. Such a strategy was used for the structure solution of the large-pore germanosilicate ITQ-26.[29] The space group ($I4/mmm$) and unit cell parameters (a = 26.7769(8) Å, c = 13.2505(5) Å) of ITQ-26 were determined from a tilt series of ED patterns. Structure factor phases were deduced from the integrated ED intensities ($hk0$ + $0kl$) by maximum entropy and likelihood[52] using the program MICE,[58] which were used as constraints for subsequent phasing trials on the PXRD data using the zeolite-specific structure solution program FOCUS.[59] The correct structure solution was identified by the electrostatic potential maps obtained from electron diffraction. The final model was refined by Rietveld methods. The structure of ITQ-26 has seven symmetry-independent T-sites. The framework contains 3D channel systems with straight 12-ring channels along [001] and two other 12-ring channels tilted with respect to the c-axis. Xie et al. applied single-crystal charge flipping algorithm[60] implemented in the program Superflip[61] and successfully obtained structure factor phases from 2D PED patterns of ZSM-5 along four zone axes.[62] 594 phases from the four projections were included in the initial phase sets of pCF runs and led to significant improvement in the resulting electron density maps.

Another strategy is to use ED intensities for pre-repartition of the overlapping reflections in PXRD. Such a strategy was applied for solving the structure of the germanosilicate ITQ-37 (space group $P4_132$ or $P4_332$, a = 26.5126(3) Å).[30] ITQ-37 is the first chiral zeolite with one single gyroidal channel system and pore openings defined by 30-ring windows. It had the lowest framework density (10.3 T-atoms/1000 Å^3) of all existing 4-coordinated crystalline oxide frameworks. The high degree of reflection overlap (>94%) made the structure solution by PXRD alone difficult. ITQ-37 was too beam sensitive to obtain high quality HRTEM images. Instead SAED patterns were taken along four different zone axes (**Figure 4**). ED intensities (d > 3.3 Å) were extracted and used for pre-repartitioning of the overlapping reflections in the PXRD pattern. The powder charge flipping (pCF) algorithm[63] was applied for the structure solution based on the improved XRD intensities after pre-repartitioning using the computer program Superflip.[61] All ten symmetry-independent Si/Ge positions and 18 out of 19 oxygen positions could be located from the best electron density map (Figure 4). The missing oxygen position could be identified and placed between two T-sites. Rietveld refinement was performed to obtain the final structure model.

3.3. Structure Determination of Zeolites by 3D Electron Diffraction Tomography – ADT and RED

The recently developed 3D electron diffraction tomography methods represented by the automated diffraction tomography (ADT) and rotation electron diffraction (RED) have been very successful in solving polycrystalline zeolite structures.[64] The structure solution methods applied on the ADT/RED data include direct methods (e.g. programs SHELX,[65] SIR[66]), charge flipping (e.g. programs Superflip,[61] Jana[67]) and simulated annealing (e.g. program SIR[66]). The structure models can be refined by full-matrix least-squares refinement using the program SHELX.[65] The kinematical approach has been applied, i.e. the ED intensities are proportional to the square of the structure factor amplitudes. Atomic scattering factors for electrons are used instead of those for X-rays. Due to the

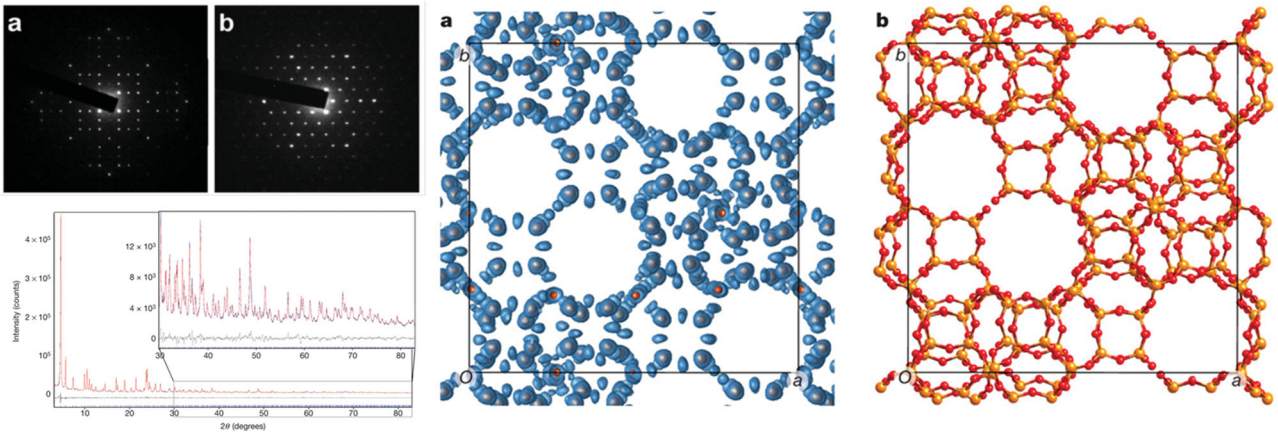

Figure 4. (Left) The SAED and PXRD patterns from ITQ-37 and (right) the electron density maps derived by the powder charge flipping (pCF) algorithm and the final structure model, viewed along *c*-axis. Reproduced with permission.[30] Copyright 2009, Macmillan Publishers Ltd.

presence of dynamical scattering, the atomic positions obtained by ADT and RED are still not as accurate as those obtained by X-ray diffraction. A better approach is to refine the structure model against PXRD data by Rietveld refinement. Here we present the structure determination of two novel zeolites ITQ-43[34] and ITQ-51,[35] solved from the ADT and RED data, respectively.

ITQ-43 (*Cmmm*, a = 26.090 Å, b = 41.866 Å, c = 12.836 Å) is a mesoporous zeolite synthesized using (2′R,6′S)-2′,6′-dimethylspiro[isoindoline-2,1′-piperidin]-1′-ium hydroxide as the OSDA. The framework contains 28-ring cloverleaf-like channels running along the *c*-axis that are interconnected by 12-ring channels.[34] The severe peak overlap and lack of high angle peaks in the PXRD pattern made it difficult to solve the structure of ITQ-43 by PXRD. ADT was used for the structure solution of ITQ-43. Two tilt series of ADT data from two different crystals were collected at ~100 K using a cryo-holder and merged for the structure solution in space group *C*222 (**Figure 5**). All the 20 independent silicon/germanium positions and 20 of 42 oxygen positions were found by direct methods using SIR2008.[66] 13 more oxygen positions were identified during the subsequent Fourier refinement. The remaining five oxygen positions were added based on the geometry. The refined structure model showed *Cmmm* symmetry. The final structure model was refined by Rietveld refinement against the PXRD data.

ITQ-51 is an extra-large 16-ring silicoaluminophosphate synthesized using the bulky aromatic proton sponges 1,8-bis(dimethylamino)naphthalenes as the OSDAs.[35] The structure was solved from submicrometer-sized crystals using the RED data. Two RED datasets from two different ITQ-51 crystals were collected and merged together (**Figure 6**). The unit cell parameters (a = 23.345(2) Å, b = 16.513(2) Å, c = 4.9814(5) Å, α = 90°, β = 90.620(5)°, γ = 90°) were determined from the RED data and further refined against the PXRD data. The space group, $P2_1/n$, was deduced from the reflection conditions. 2310 independent reflections with the completeness of 81.8% (d > 0.9 Å) were obtained from the merged RED dataset. All eight symmetry independent framework T (Al, Si, P) atoms and 16 oxygen atoms could be located by direct methods using the RED data. The structure model could be refined against the RED intensities ($R1$ = 0.37) and showed reasonable geometry. The Al and P positions could be assigned based on the difference in the Al-O and P-O bond distances. The structure model was further refined by Rietveld refinement against the PXRD data. The atomic positions obtained from the RED data (as-made ITQ-51 sample) deviated on average by 0.11 Å for Al/P and 0.13 Å for O from those obtained by the Rietveld refinement (calcined ITQ-51 sample). This means that RED can give a very good starting model. The high $R1$-value was probably due to the multiple scattering.

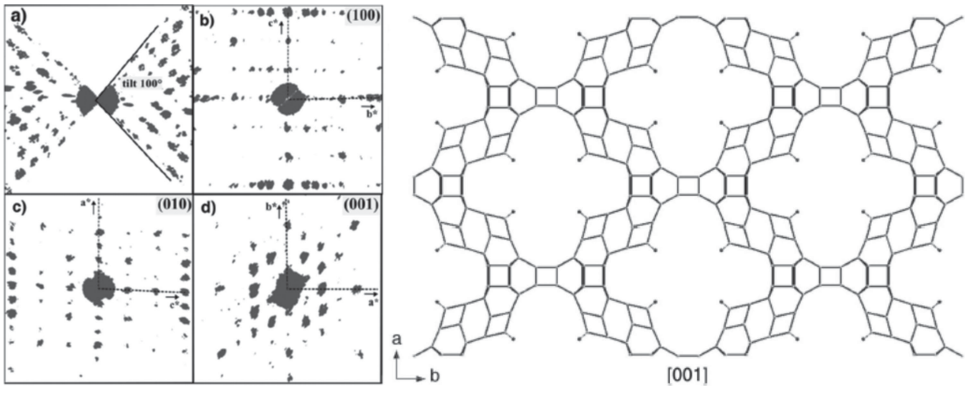

Figure 5. (Left) 3D projections of the reconstructed reciprocal lattice of ITQ-43 from the ADT data viewed along a) the tilt axis, b) the $\boldsymbol{a}^*$-axis, c) the $\boldsymbol{b}^*$-axis and d) the $\boldsymbol{c}^*$-axis. (Right) Structure model of ITQ-43 viewed along the *c*-axis. Reproduced with permission.[34] Copyright 2011, AAAS.

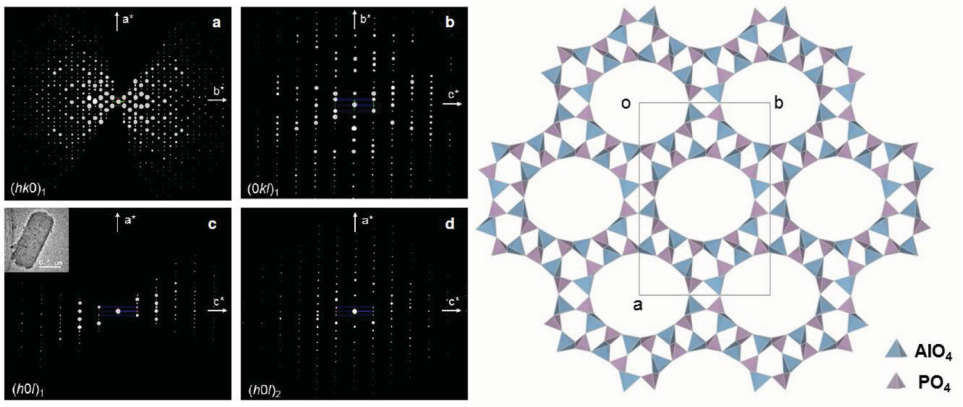

Figure 6. (Left) 2D slices of the reciprocal lattice of ITQ-51 reconstructed from the 3D RED data. (a-c) 2D slices from the dataset 1. The crystal is shown as an insert in (c). (d) 2D (h0l) slice from the dataset 2, showing that the two datasets cover different parts of reciprocal space. (Right) Structure model for ITQ-51 viewed along the *c*-axis. Adapted with permission.[35] Copyright 2013, National Academy of Sciences.

4. Structure Determination of Zeolites by High Resolution Transmission Electron Microscopy (HRTEM)

HRTEM has been essential for structure solution of many zeolites which couldn't be solved by X-ray diffraction, because the crystals are too small, and/or the samples contain impurity or disorders. The early efforts of structure solution of zeolites have been by combining HRTEM images with model building. During the past years, a number of complex zeolite structures have been solved by combing HRTEM with PXRD, where the structure factor phases obtained from HRTEM images have been the key for the structure solution. A more general approach of solving zeolite structures is by 3D reconstruction of HRTEM images taken from different zone axes, which has been used successfully to solve complex zeolite structures. The 3D reconstruction method is especially useful for solving disordered zeolites, which give poor PXRD patterns with broad peaks. We will review these different approaches to solve zeolite structures by HRTEM below.

4.1. Structure Determination of Zeolites by Combining HRTEM and Model Building

Many zeolite structures were solved by model building based on HRTEM images taken from one or several projections, such as zeolite beta (*BEA),[68,69] SSZ-26/SSZ-33 (CON),[70] SSZ-31 (*STO),[71] ITQ-38,[31] MCM-22 (MWW),[72] Ti-YNU-1,[73] ETS-10,[74] UTD-1 (DON),[75] and ITQ-15 (UTL).[76] Model building has been especially useful for zeolites containing stacking disorders. Knowing the various types of stacking disorders in zeolites and the characteristic features in the corresponding diffraction patterns is therefore important for solving unknown zeolites containing stacking disorders. A recent review by us summarized the structure elucidation and analysis of stacking disorders in zeolites and open-frameworks by electron crystallography and X-ray diffraction.[77]

Zeolite beta possesses 3D intersecting 12-ring channels and is an intergrowth of two beta polytypes A and B. The polytypes A and B are built from the same layer but with different layer stackings. The structure model of zeolite beta was proposed in 1988 by Treacy et al.[68] and Higgins et al.[69] 4-, 5-, 6- and 12-rings as well as the pore stacking sequences were identified from HRTEM images, from which a structure model was derived. There exist two types of pore stackings, ABAB... and ABCABC..., with the shift of one-thrid of the intralayer pore spacing.[68] SSZ-26 and SSZ-33 belong to a family of zeolites with 3D intersecting 10- and 12-ring channels.[70] SSZ-26 is an aluminosilicate analogue in the family while SSZ-33 is a borosilicate analogue. Both materials have stacking disorders and are constructed from the same framework building layer. The building layers, aligned in the ***ab***-plane, stack along the ***c****-axis with a shift of either +1/3***b*** or -1/3***b***. It is the intergrowth of two polytypes A and B, with the pore stacking of ABAB... and ABCABC, respectively. SSZ-31 is a family of high-silica zeolite materials containing 1D 12-ring channels along the ***b***-axis. The structure was solved by Lobo et al. combining adsorption measurements, electron diffraction, HRTEM and PXRD.[71] SSZ-31 can be described either as an intergrowth of four different but structurally related polytypes, or by different connection modes of parallel 12-ring channels constructed by rolled up honeycomb-like sheets of fused 6-rings.

MCM-22 (MWW, space group *P*6/*mmm*, a = 14.1145(8) Å, c = 24.8822 Å) is a high silica zeolite built of MWW double layers and consists of two non-intersecting 10-ring channel systems and side pockets with 12-ring openings.[72] The structure model was derived from two HRTEM images taken along [001] and [100] and refined against synchrotron diffraction data. MCM-22 is one of the most important and industrially used zeolite catalysts. The titanosilicate Ti-YNU-1 ($a = b$ = 14.238 Å, c = 27.571 Å) was prepared from an MWW-type precursor and has an interlayer expanded 3D MWW-type framework. HRTEM images indicated that the connection of the MWW sheets was expanded, and the pores within the interlayers were enlarged from 10-rings to 12-rings compared to the 3D MWW framework.[73] Ti-YNU-1 shows a significantly higher intrinsic catalytic activity than 3D Ti-MWW and 12-ring Ti-Beta in the epoxidation of bulky alkenes with H_2O_2. The structure of Ti-YNU-1 has two-connected $Si(OH)_2$ groups and is thus not strictly a

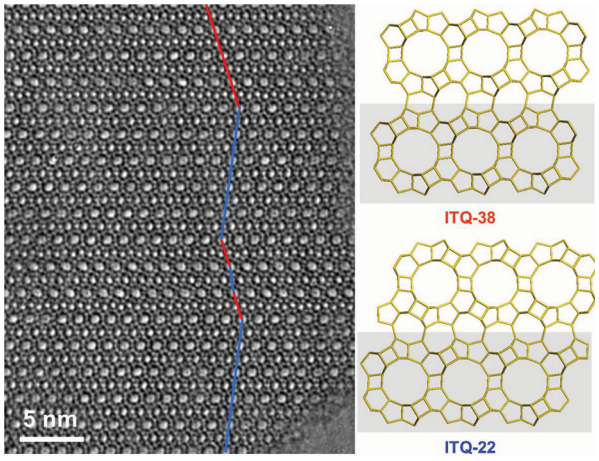

Figure 7. Structure projection of ITQ-38 along [010] reconstructed from 20 HRTEM images of a through-focus series, showing the intergrowth of ITQ-38 (traced by blue lines, with 10- and 12-ring) with ITQ-22 (traced by red lines, with 8- and 12-rings). ITQ-38 and ITQ-22 are built from the same building layers (shaded) which are connected differently. Adapted with permission.[31] Copyright 2012, American Chemical Society.

zeolite. ETS-10 is another titanosilicate, which was solved by combination of HRTEM, electron diffraction, XPRD, solid-state NMR, chemical analysis and model building.[74] The ETS-10 material is disordered and can be described as an intergrowth of two different polytypes A and B, both are built from the same layer. ETS-10 contains 3D interconnected 12-ring channels built by SiO_4 tetrahedra and TiO_6 octahedra.

Recently we reported the struture of a new germanosilicate ITQ-38 ($P2/m$, $a = 13.02$ Å, $b = 12.70$ Å, $c = 21.25$ Å, $\beta = 96.87°$) with 10- and 12-ring channels along [010] and 10-ring channels along [100] and [101].[31] ITQ-38 was synthesized using the dicationic piperidine-derivatives as the OSDAs. It could be found both as perfect crystals and as intergrowth with ITQ-22 (IWW). Because ITQ-38 was very beam sensitive, low dose conditions were applied and the structure image (**Figure 7**) was reconstructed from a through-focus series of 20 HRTEM images using the software QFocus[43] to enhance the signal to noise level. The structure of ITQ-38 was solved from HRTEM images taken along [010] and [101]. The frameworks of both ITQ-22 and ITQ-38 are built from the same building layer, see Figure 7. There are two possible ways to connect the layers, where the neighboring layers are related either by an inversion center as in ITQ-38 or by a glide plane as in ITQ-22.

UTD-1 is a disordered high-silica zeolite containing 1D 14-ring channels, synthesized using bis(pentamethylcyclopentadienyl) cobalt(III) hydroxide as the structure directing agent. The structure was derived from modeling building based on HRTEM images. The disorder arises from different up/down configurations of the SiO_4 tetrahedra. ITQ-15 is a germanosilicate synthesized using 1,3,3-trimethyl-6-azonium-tricyclo-[3.2.1.$4^{6,6}$] dodecane as the OSDA. The structure solution was achieved by combining TEM, XRD and energy minimization calculations.[76] The starting model was deduced from HRTEM images along different projections. The framework of ITQ-15 possesses an interconnected 14-ring and 12-ring channels. The catalytic results showed the benefit of the pore structure of ITQ-15 compared with unidirectional pore zeolites (UTD-1).[75] The framework structure of ITQ-15 is the same as IM-12,[78] which was independently solved from PXRD data by direct methods.

4.2. Structure Determination of Zeolites by Combining HRTEM and X-ray Diffraction

High resolution electron microscopy and powder X-ray diffraction are complementary. Complete and kinematical PXRD data can be obtained easily while the acquisition of HRTEM images is very time consuming. The structure factor phase information obtained from HRTEM images can facilitate the ab initio structure solution processes by PXRD. Several most complex zeolite structures were solved by combining HRTEM and PXRD, such as TNU-9 (TNU),[26] IM-5 (IMF)[27] and SSZ-74 (-SVR).[28] HRTEM was also combined with single crystal X-ray diffraction to solve the structure of a disordered germanosilicate SU-78.[36]

TNU-9 ($C2/m$, $a = 28.2219$ Å, $b = 20.0123$ Å, $c = 19.4926$ Å, $\beta = 92.33°$) is a high silica zeolite with 3D 10-ring channels, synthesized using 1,4-bis(*N*-methylpyrrolidinium)-butane and Na^+ ions as the structure directing agents.[26] The structure was solved using the zeolite-specific structure solution program FOCUS.[15] The key to the success was the use of the structure factor phases (in total 258) obtained from HRTEM images taken along three projections as starting phases.[26] The structure of TNU-9 contains 24 symmetry-independent T-atoms and was then the most complex zeolite structure solved. Compared to other zeolite catalysts, TNU-9 showed unique shape selectivity in acid-catalyzed reactions.

IM-5 is a high silica zeolite with 2D 10-ring channels, synthesized using 1,5-bis(*N*-methylpyrrolidinium)-pentane as the OSDA. It is an active catalyst for hydrocarbon cracking and NO reduction. Due to the severe peak overlap, the structure ($Cmcm$, $a = 14.299$ Å, $b = 57.413$ Å, $c = 20.143$ Å) could not be solved from PXRD data alone using standard ab initio structure solution methods such as FOCUS[15] or powder charge flipping (pCF).[63] The unit cell parameters were determined from a tilt series of SAED patterns using the program Trice.[79] HRTEM images along the three main zone axes of IM-5 were taken (**Figure 8**a–c), from which the projection symmetry and the structure factor amplitudes and phases were extracted using the program CRISP.[41] 95 structure factors obtained from the three HRTEM images were used to reconstruct a 3D electrostatic potential map, from which an initial structure model was obtained. However, the model deviated to some extent from the final structure and could not be refined by PXRD. When the 95 structure factor phases calculated from the initial structure model were included as the starting phase sets in pCF[63] implemented in the program Superflip,[61] a better structure model could be obtained from the electron density map (Figure 8). The structure model could be finally refined against the PXRD data using the Rietveld method. IM-5 also contains 24 symmetry independent T-atoms and has an unusual 2D medium pore channel system. It was shown later that the complex structure of IM-5 could also be solved by 3D reconstruction from HRTEM images alone.[80]

SSZ-74 is a high silica zeolite with 3D 10-ring channels, synthesized using 1,6-bis(*N*-methylpyrrolidinium)-hexane as

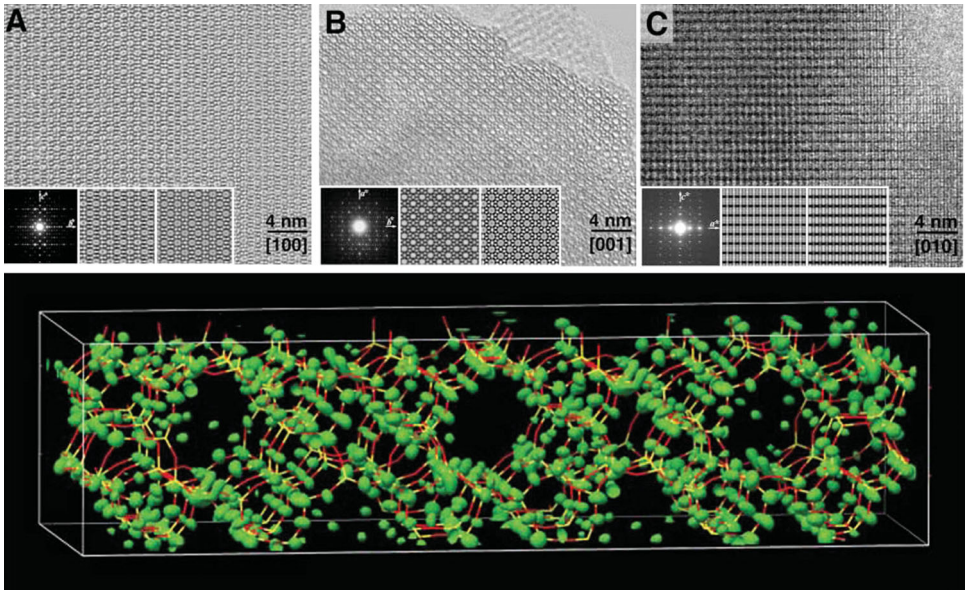

Figure 8. (Above) HRTEM images of IM-5 taken along (a) [100], (b) [001] and (c) [010]. (Below) The electron density map (in green) obtained after pCF is with the final structure model superimposed. Reproduced with permission.[27] Copyright 2007, AAAS.

the OSDA. The structure ($C2/c$, a = 20.514 Å, b = 13.395 Å, c = 20.097 Å, β = 102.2°) was solved by PXRD using the information from one HRTEM image.[28] A structure envelope was generated from 20 structure factors obtained from this HRTEM image, which defines where the pores should be located in the unit cell and where framework atoms should be. The structure model was obtained from the PXRD data using the pCF algorithm implemented in the program Superflip,[63] where the structure envelope was imposed in real space to eliminate any electron density in the pore regions. The structure of SSZ-74 has ordered vacancies which were not observed before in zeolites.

Single crystal X-ray diffraction (SXRD) is a powerful technique to solve crystal structures, but it can sometimes encounter difficulties when the structures are disordered. SU-78 is a germanosilicate synthesized by employing dicyclohexylammonium hydroxides as the OSDAs.[36] Although the crystals were large enough (10 µm × 10 µm × 30 µm) for single crystal X-ray diffraction on the synchrotron, the SXRD data showed streaks for reflections with indices $h = 3n \pm 1$ and sharp spots for reflections with indices $h = 3n$. A 2D charge flipping algorithm was applied to the sharp spots of the $0kl$ reflections to generate a projected electron density map along [100]. The streaks in the $h0l$ plane correspond to the presence of stacking disorders, which was confirmed by HRTEM images along [010]. By combining the structure information along [100] from SXRD and those along [010] from HRTEM, a structure model of SU-78 could be built (**Figure 9**).[36] SU-78 is an intergrowth

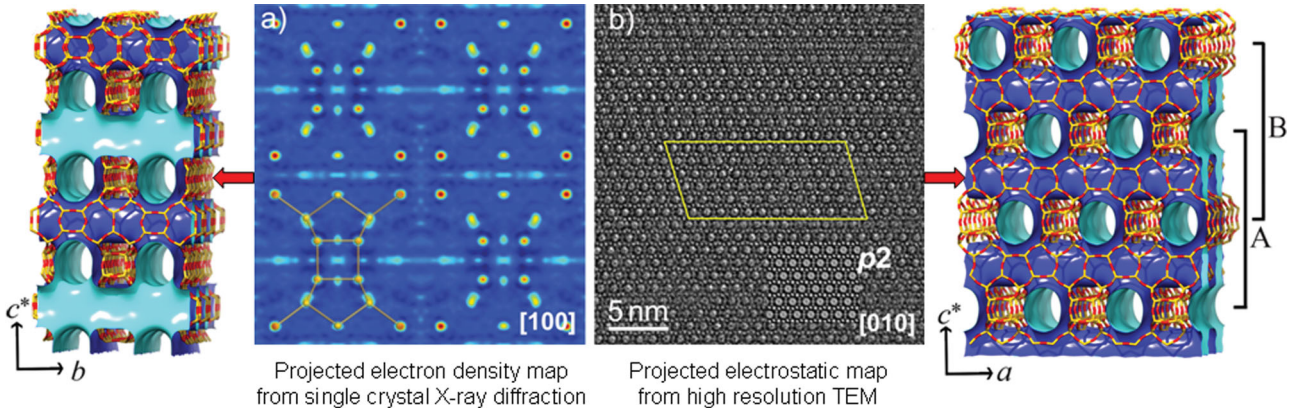

Figure 9. Illustration of the structure of SU-78 solved by combinating single crystal X-ray diffraction and HRTEM. Electron density projected along [100] was obtained by 2D charge-flipping from the X-ray diffraction data and resembles the projection of beta polytype C. The HRTEM image taken along [010] is similar to that of zeolite beta with stacking disorders. A 3D structure model was built by combining the two projections. The resulting structure model of SU-78 shows the BEC-type channels along [100] and the beta-type channel systems [010]. The cyan surfaces are towards the pores while the blue surfaces are towards the framework. The parts with SU-78A and SU-78B are marked. Adapted with permission.[36] Copyright 2012, American Chemical Society.

of two polytypes SU-78A and SU-78B and contains interconnected 12-ring channels in three directions. The two polytypes are built from the same building layer, similar to those in the zeolite beta family. However, the layer stacking in SU-78 is different from those in zeolite beta polytypes A, B, and C. SU-78 turned out to be an intergrowth of two new polytypes of zeolite beta, which was previously proposed as polytypes D and E.[81]

4.3. Structure Determination of Zeolites by 3D Reconstruction of HRTEM Images

A more general method to solve unknown zeolite structures is by 3D reconstruction of HRTEM images. Structure factor amplitudes and phases were extracted from HRTEM images along different projections and combined into a 3D electrostatic potential map, as described in Section 2.3. 3D reconstruction has been used to solve the structures of the high-silica zeolite beta polytype C (BEC)[82,83] and polytype B.[84] It has been recently used to solve the structure of an intergrown zeolite ITQ-39.[32,85]

Zeolite beta polytype C (BEC) was first synthesized by our group as a pure germanate using 1,4-diazabicyclo-[2,2,2]-octane as the OSDA.[86] Its structure was solved by single crystal X-ray diffraction. A pure silica BEC ($P4_2/mmc$, a = 13.1 Å, c = 13.8 Å) was observed by HRTEM as overgrown pillars on zeolite beta crystals.[82] A 3D electrostatic potential map was obtained by 3D reconstruction from HRTEM images along [001] and [100], from which some of the Si positions could be identified. In order to confirm the Si positions, an independent structure solution using intensities extracted from SAED patterns along seven different zone axes was conducted by the Patterson method. The final structure model was deduced.[83]

Corma and co-workers synthesized a highly enriched form of zeolite beta polytype B using 4,4-dimethyl-4-azonia-tricyclo[5.2.2.02,6]undec-8-ene hydroxide as the OSDA. SAED showed that all crystals contained twins of beta polytype B. The unit cell parameters (a = 17.97 Å, b = 17.97 Å, c = 14.82 Å, β = 113.7°) were determined from a tilt series of SAED patterns using the program ELD[47] and Trice.[79] The space group ($C2/c$) was deduced from the systematic absences and HRTEM images. The HRTEM image taken along [1-10] clearly shows 12-ring channels arranged in an ABCABC... stacking sequence characteristic for polytype B (**Figure 10**). Structure factor amplitudes and phases of 39 symmetry-independent *hhl* reflections were extracted from the HRTEM image using the program CRISP[41]. Because the *h-hl* and *-hh-l* reflections in the [110] projection are symmetry-related to the *hhl* and *-h-h-l* reflections in the [1-10] projection, their amplitudes and phases could be deduced from those of *hhl* and *-h-h-l* reflections. In such a way 152 structure factors could be generated, from which a 3D electrostatic potential map could be constructed. All the 9 independent Si atoms could be located from the 3D potential map (Figure 10).[84] This example demonstrates that a 3D structure can be solved from one single projection, if the symmetry of the crystal is utilized.

The structure of the aluminosilicate ITQ-39 was solved by electron crystallography from crystal domains only a few unit cells in size.[32] ITQ-39 is an intergrowth of three different polytypes (ITQ-39A, ITQ-39B and ITQ-39C), built from the same layer but with different stacking sequences. ITQ-39 contains stacking faults and twinning with nano-sized domains, being the most complex zeolite ever solved. Because several types of disorders were present simultaneously in the ITQ-39 crystals, it was necessary to obtain complete 3D data from the same crystal in order to find the orientation and relation of the disorders, and determine the unit cells. A 3D RED dataset with 880 SAED patterns was collected with 0.15° interval between the consecutive ED frames from one single crystal. Twining and stacking disorders could be identified from two perpendicular 2D cuts of the 3D reciprocal lattice reconstructed from the RED data, see **Figure 11**a,b. The 3D RED data revealed that the different ITQ-39 polytypes share two common axes, ***a*** and ***b***. HRTEM images were thus collected along these two common axes ***a*** and ***b***, because they allow the observation of possible channels in a faulted sample. A through-focus series of 20 HRTEM images were acquired along each of the two axes and used to reconstruct the structure projections (Figure 11c,d). Pair-wise 12-ring channels and the twinning can be found from the image along [010] (Figure 11c). 10-ring channels and the stacking faults can be easily identified from the image along [100] (Figure 11d). The ordered crystal domains in ITQ-39 are only a few unit cells in size. Structure factor amplitudes and phases were extracted from the Fourier transforms of the ordered regions of ITQ-39B. A 3D electrostatic potential map of ITQ-39B was reconstructed from the 53 strongest reflections (with amplitudes > 8% of the largest amplitude). All 28 unique Si atoms could be located from the 3D map, see Figure 11e. The structures of two other polytypes ITQ-39A and ITQ-39C

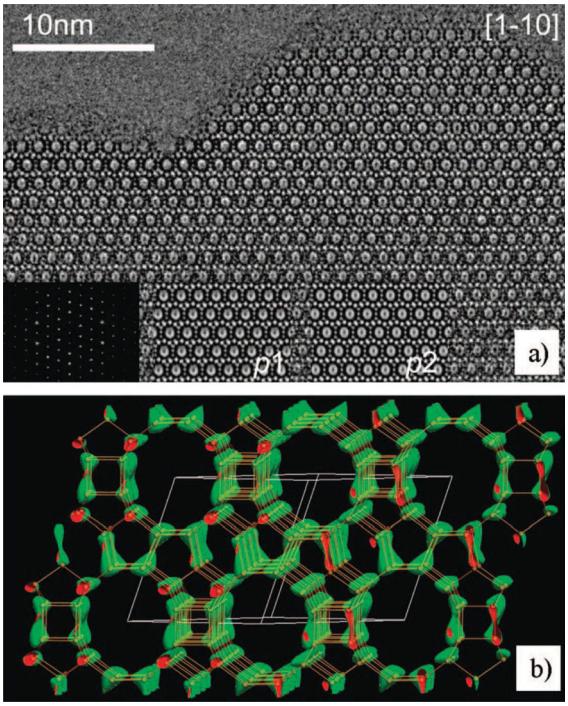

Figure 10. (a) An HRTEM image of polytype B enriched beta taken along the [1-10] direction. (b) The 3D electrostatic potential map constructed from the [1-10] HRTEM image by utilizing the crystal symmetry. Adapted with permission.[84] Copyright 2008, American Chemical Society.

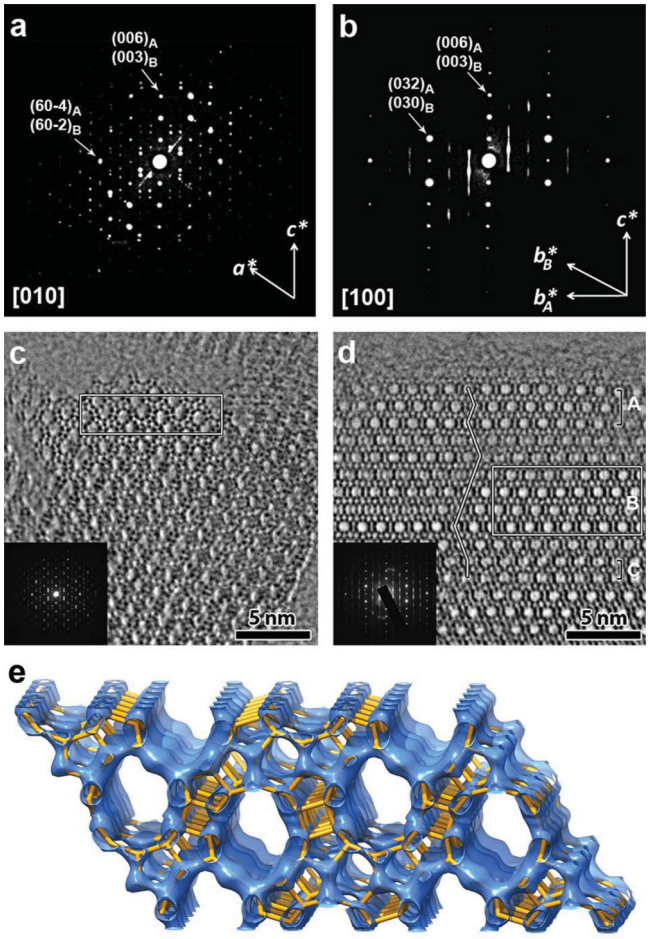

Figure 11. (a-b) Two perpendicular cuts of the reconstructed 3D reciprocal lattice of ITQ-39 from the RED data from one single crystal. (a) the *h*0*l* slice and (b) the 0*kl* slice. The *h*0*l* pattern can be indexed using two twin components A and B. The 0*kl* pattern can be indexed using two different lattices, corresponding to ITQ-39A and ITQ-39B. (c-d) Structure projection images reconstructed from 20 HRTEM images along (c) [010] and (d) [100]. Twins can be identified from the orientation of the pair-wise 12-ring channels in (c). 10-ring channels are observed in (d) and the channel stacking is traced by a line. The different stacking leads to three polymorphs ITQ-39A, ITQ-39B and ITQ-39C. The domains used for structure factor determination are outlined by rectangles. (e) The 3D electrostatic potential map of ITQ-39B reconstructed from the structure factor amplitudes and phases extracted from the marked nano-domains in (c) and (d). All 28 symmetry-independent Si atoms could be located directly from the 3D map. The refined structure model of ITQ-39 is superimposed. Reproduced with permission.[32] Copyright 2012, Macmillan Publishers Ltd.

were constructed based on the stacking sequences found in Figure 11d. The structures were geometrically refined and confirmed by simulated PXRD patterns. The structure of ITQ-39 contains straight pair-wise 12-ring channels along *b*, which are interconnected by three 10-ring channels. The pair-wise 12-ring channels are unique and have not been observed in any other zeolites. The unique pore topology makes ITQ-39 a promising catalyst for alkylation of aromatics with olefins, which is especially useful for conversion of naphata to diesel fuel, a process of emerging interest for the petrochemical industry.

5. Structure Determination of Metal-Organic Frameworks by 3D Electron Diffraction Tomography and HRTEM

Metal-organic frameworks are less stable than zeolites under electron beam. 3D electron diffraction tomography made it possible for the first time to collect 3D electron diffraction data of MOF crystals. Both ADT and RED data have been used for solving MOF structures, such as ZIF-7, MFU-4[87] and CAU-7.[88]

The zeolitic imidazolate framework ZIF-7 was used as a test sample to study the feasibility of structure solution of MOFs by the RED method. ZIF-7 is a Zn-MOF with the composition $[Zn(bIm)_2 \cdot 3H_2O]$ (bIm = benzimidazolate) and was synthesized from $Zn(NO_3)_2 \cdot 6H_2O$ and benzimidazole.[89] The RED data was collected at ~90 K using a cryo-holder in order to reduce the beam damage. 552 ED frames were collected from +27.01° to -21.25° with a beam tilt step of 0.1° and exposure time of 3.0 s per ED frame (**Figure 12**a). 131 symmetry-independent reflections (d > 1.43 Å) were obtained. The unit cell parameters (a = 22.47 Å, c = 15.86 Å) and space group (*R-3*) could be directly determined from the 3D reciprocal lattice reconstructed from the RED data. All the zinc and nitrogen positions could be located directly by direct methods implemented in SHELX[65] using the RED data (Figure 12b). The carbon positions could not be found, and were introduced manually according to the geometry of the bIm linker. The structure model could be refined against the RED data ($R1$ = 0.28) using soft restraints of the bond distances and bond angles.

MFU-4 is a Zn-MOF $[Zn_5Cl_4(BTDD)_3]$ (H_2-BTDD = bis(1H-1,2,3-triazolo[4,5-b],-[4′,5′i])dibenzo[1,4]dioxin). The ADT data with and without precession were collected at ~110 K using a cryo-holder. The space group (*Fm-3m*) and unit cell (a = 31.057 Å) were determined from the ADT data without precession. 412 independent reflections up to a resolution of 1.3 Å were integrated from the ADT data with precession. Ab initio structure solution was performed by direct methods implemented in SIR2008.[66] Nine out of the ten unique positions could be located; only one carbon position could not be located. MFU-4l contains two different cavities with the free diameter of 11.97 Å and 18.56 Å, respectively. It is the first unknown MOF structure solved by electron crystallography.[87]

CAU-7 is a bismuth-based MOF Bi(BTB) (BTB = 1,3,5-benzenetrisbenzoate). The ADT data showed that each CAU-7 crystal is a twin aggregate of three individuals that grow following the pseudohexagonal symmetry of the structure. The unit cell parameters (a = 32 Å, b = 28 Å, c = 4 Å) and extinction group (*Pb-a*) were obtained from the reconstructed ADT datasets. ADT datasets from two different single twin domains were merged together and 1158 independent reflections were obtained with the resolution of 1.15 Å (**Figure 13**). Only the bismuth atom could be located by direct methods using the ADT intensities. Simulated annealing (SA) implemented in SIR2011[66] was used instead. One bismuth atom and one BTB were input in the unit cell, and a reasonable structure solution was obtained based on the ADT intensities. Finally, the structure model was refined by Rietveld refinement against the PXRD data. DFT-based calculation was performed to confirm the model.[88]

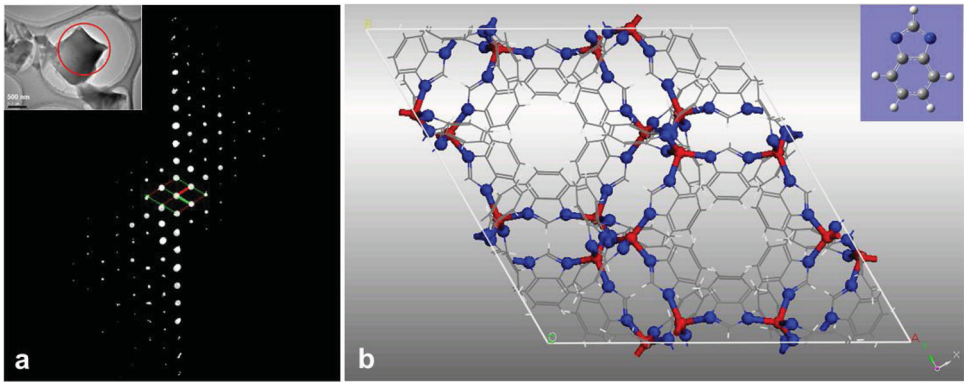

Figure 12. (a) Reconstructed 3D reciprocal lattice of ZIF-7 from the RED data. Insert is the crystal of ZIF-7 from which the RED data was collected. (b) The structure model of ZIF-7 refined from the RED data. All Zn and N atoms (highlighted in b) could be located by direct methods using the RED data. The structure of the benzimidazolate is inserted.

Like zeolites, defects can also be present in MOF crystals. Information about the defects can lead to a better understanding of crystal growth mechanisms and properties of the MOFs. The defects are difficult to identify by X-ray diffraction and electron diffraction. HRTEM can provide direct evidence of the structure as well as defects in MOF crystals. However, it is challenging to get good HRTEM images on MOFs due to the beam damage. Zhou and co-workers successfully obtained HRTEM images of a non-porous MOF Cu-SIP-3-pyridine·H_2O [$Cu_2(OH)(C_8H_3O_7S)(C_5H_5N)\cdot H_2O$], which confirmed the structure of Cu-SIP-3-pyridine·H_2O obtained by single crystal X-ray diffraction.[90] The presence of defects in the Cu-SIP-3-pyridine·H_2O crystals were also observed. Another example of HRTEM studies of MOFs is on Ni-CAT-1, which was synthesized by Yaghi's group.[91] Ni-CAT-1 is one of the two isostructural metal catecholates (Cu-CAT-1 and Ni-CAT-1) built of Ni ions and the highly conjugated tricatecholate 2,3,6,7,10,11-hexahydroxytriphenylene. Cu-CAT-1 and Ni-CAT-1 have high chemical stability, thermal stability, and porosity. The Cu-CAT-1 microcrystalline material showed high electrical conductivity and charge storage capacity. Terasaki et al. applied HRTEM, STEM imaging and electron energy loss spectroscopy (EELS) to an activated Ni-CAT-1 sample (**Figure 14**).[91] The HRTEM images confirmed that the channels in Ni-CAT-1 were along the *c*-axis and arranged in a uniform honeycomb structure. Defects could be also observed in the HRTEM images, as indicated by the arrow in Figure 14B. In addition, terminal structures of the Ni-CAT-1 can be clearly observed (Figure 14C).

HRTEM has also been used to observe the arrangement of channels in the isoreticular series of the MOF-74 family.[92] Yaghi's group expanded the pore size of MOF-74 by replacing its original link of one phenylene ring (I) to two, three, four, five, six, seven, nine, and eleven (II to XI, respectively), (termed IRMOF-74-I to XI) with pore apertures ranging from 14 to 98 Å. HRTEM images showed the presence of both ordered hexagonal arrangement of the 6-ring channels and defects with 4- and 8-ring channels. The pore apertures of an oligoethylene

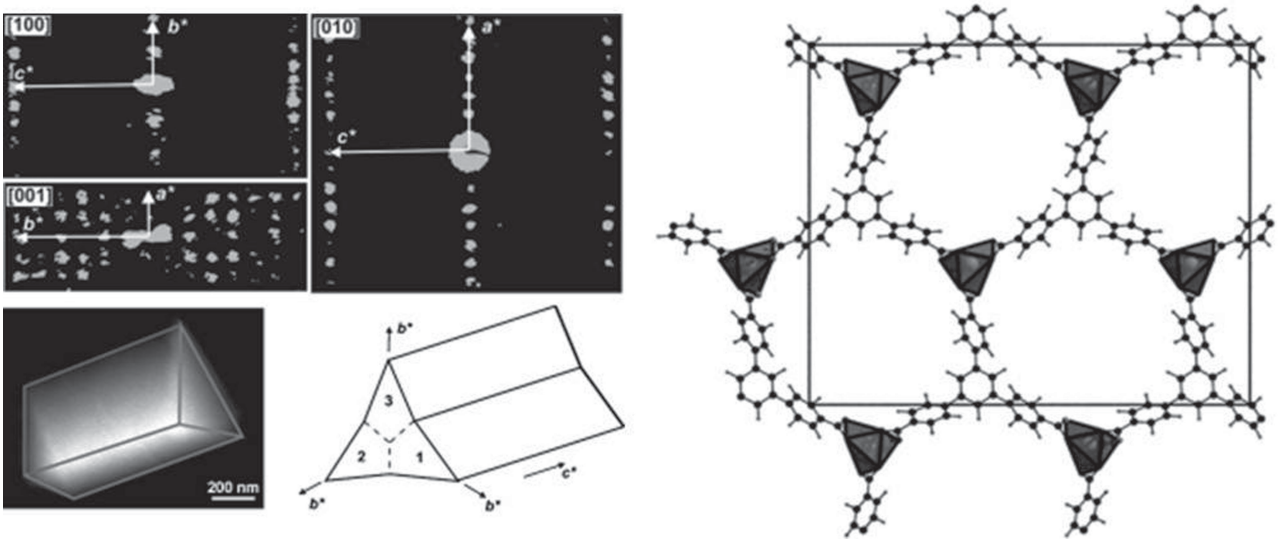

Figure 13. (Top left) Reconstructed 3D diffraction space of CAU-7 projected along the main axis directions. (Bottom left) A rod tilted to expose the triangular base and (bottom right) a sketch of the trilling arrangement. (Right) The refined structure model of CAU-7. Reproduced with permission.[88]

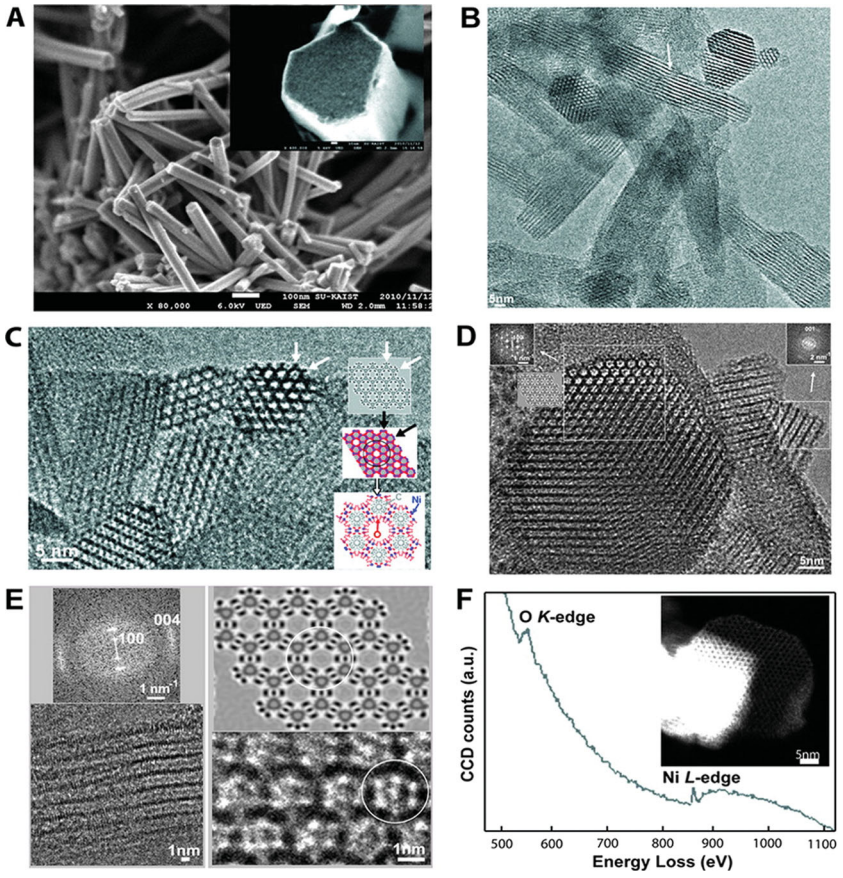

Figure 14. (A) FE-SEM image of Ni-CAT-1. (B) Low-magnification HRTEM image of the activated Ni-CAT-1 taken at 120 kV. (C) High-magnification HRTEM image showing the terminal structure of activated Ni-CAT-1 as indicated by arrows. (D) High magnification HR-TEM image of Ni-CAT-1 taken at 120 kV, the insets are the Fourier transforms (FTs) of the corresponding areas indicated by the arrows. (E) HRTEM image and corresponding FT demonstrating the wavy characterization of the edges perpendicular to the pore walls (left) and the comparison between the HRTEM and simulated images viewed along [001] (right). (F) Electron energy loss spectroscopy (EELS) spectrum with the HAADF image taken at 60 kV. Adapted with permission.[91] Copyright 2012, American Chemical Society.

glycol–functionalized IRMOF-74-VII and IRMOF-74-IX are large enough to accommodate natural proteins.

6. Structure Determination of Ordered Mesoporous Materials by Electron Crystallography

The class of ordered mesoporous materials was discovered independently by the Mobil scientists[93] and Japanese scientists.[94] Mesoporous materials have ordered pore structures in the mesoscale, but disordered wall structures at the atomic scale. Thus, PXRD of ordered mesoporous materials gives only few low-angle diffraction peaks, which are not enough for solving the structures. Electron crystallography is a unique technique for structural studies of such mesoporous materials, because much more reflections can be obtained from HRTEM images. Both amplitudes and phases of reflections can be extracted from the Fourier transforms of the HRTEM images and used for 3D reconstruction of the pore structures. A large number of ordered mesoporous materials have been solved from HRTEM images. The first one was the cubic MCM-48 structure with a bicontinuous pore system that follows the gyroid minimal surface.[95] Soon after another cubic SBA-6 structure with two types of cage-like pores was solved from HRTEM images.[96] Another bicontinuous mesoporous material AMS-10 was solved by 3D reconstruction of HRTEM images from three different projections.[97] The material FDU-12 is built from a face-centered packing of spherical cages, each of them connected to 12 nearest neighbors. The pore shape, pore diameter and the size of the cage entrance could be changed by changing the synthesis and hydrothermal treatment temperatures. These changes were studied by comparing the 3D potential maps reconstructed from HRTEM images of the FDU-12 materials synthesized at different temperatures.[98]

The first tricontinuous mesoporous material IBN-9 was synthesized using a specially designed surfactant and its pore structure was determined by electron crystallography.[99] Three HRTEM images of IBN-9 taken along [001], [100] and [1–10] were collected (**Figure 15**a–c). The unit cell parameters (hexagonal, $a = 88.4$ Å, $c = 84.3$ Å) were determined from the Fourier transforms of the HRTEM images. The symmetry of each projection (plane group) was determined from the HRTEM image. The space group of IBN-9 was uniquely determined from the plane groups of the three projections to be $P6_3/mcm$. The 3D electrostatic potential map was reconstructed by combining the structure factors extracted from the HRTEM images (Figure 15d). IBN-9 exhibits a unique tri-continuous structure with three identical and interwoven mesoporous channel systems separated by a single continuous silica wall (Figure 15e). Using IBN-9 as a "hard-template", mesostructured carbon and Pt materials were synthesized. The structure of the IBN-9 carbon replica was determined by 3D reconstruction from HRTEM images taken along [001], [100] and [1-10]. It consists of three 3-D interpenetrating carbon networks showing an almost perfect "negative replica" of IBN-9.[100]

7. Conclusions

In this review, we have presented different electron microscopic techniques for structure determination of unknown zeolites, metal-organic frameworks and ordered mesoporous materials. Recently several methods, i.e. the structure projection reconstruction from through-focus series of HRTEM images,[43] automated diffraction tomography (ADT)[39] and rotation electron diffraction (RED)[40] have been developed to make structure

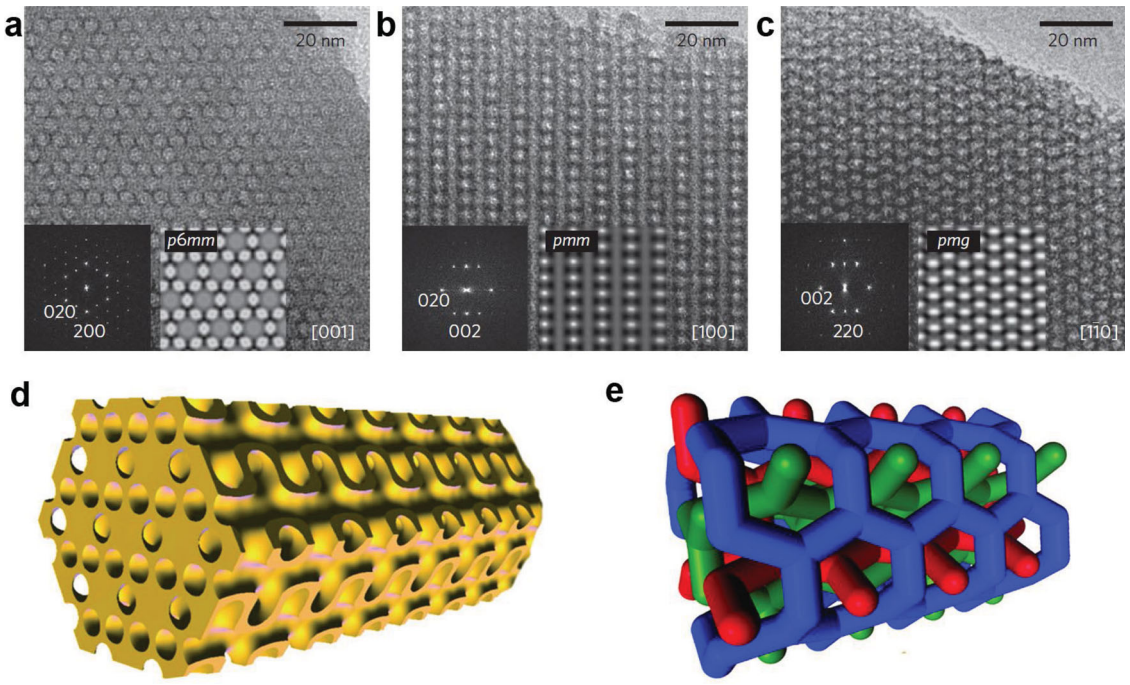

Figure 15. HRTEM images of IBN-9 taken along (a) the [001] direction, (b) the [100] direction and (c) the [1$\bar{1}$0] direction. The inserts are the corresponding Fourier transforms and the projected potential maps obtained by crystallographic image processing. (d) The 3D pore structure of IBN-9 reconstructed from HRTEM images. (e) The three separate channel systems represented by rod networks in different colors. Reproduced with permission.[99a,b] Copyright 2009, Macmillan Publishers Ltd., (a-c) and Copyright 2011, Elsevier (d-e).

determination by electron crystallography more feasible, even for non-TEM experts. The ADT and RED methods have shown to be very powerful and efficient in solving structures of unknown zeolites and metal-organic frameworks. HRTEM has unique advantages for studying disordered structures which are difficult to be studied by other techniques. The structure projection reconstruction from through-focus series of HRTEM images using the program QFocus[43] makes it easier to obtain high quality structure images. It also enhances the image contrast for especially beam sensitive materials and materials containing defects. The crystallographic structure factor amplitudes and phases can be obtained from HRTEM images and used for reconstruction of the 3D electrostatic potential map, from which the 3D structure can be determined. The phase information from HRTEM images can also be used to assist the structure solution of complex zeolites from powder X-ray diffraction. Electron crystallography and PXRD are complementary for structure analysis of porous materials. PXRD patterns contain information about the bulk sample; while electron crystallography provides detailed information on individual crystalline particles down to the nanometer sizes. The development of ADT and RED methods is revolutionary and has turned a transmission electron microscopy into a single crystal diffractometer. This makes the collection of 3D single crystal diffraction data on a TEM almost as feasible and fast as that on a single crystal X-ray diffractometer, but from crystals millions times smaller. Finally we want to emphasize that the electron crystallographic methods presented here are general and can also be used for structural studies of other functional materials.

Acknowledgements

We thank all the collaborators for their contributions to the scientific results reviewed here. This work was supported by the Swedish Research Council (VR), the Swedish Governmental Agency for Innovation Systems (VINNOVA), and the Knut & Alice Wallenberg Foundation through a grant for purchasing the TEM and the project grant 3DEM-NATUR.

Received: June 6, 2013
Published online: August 23, 2013

[1] M. E. Davis, *Nature* **2002**, *417*, 813.
[2] a) C. Baerlocher, L. B. McCusker, D. H. Olson, *Atlas of zeolite framework type,* Elsevier, Amsterdam **2007**; b) http://www.iza-structure.org/databases/, accessed April, 2013.
[3] a) G. Férey, *J. Solid State Chem.* **2000**, *152*, 37; b) M. V. Peskov, X. D. Zou, *J. Phys. Chem. C* **2011**, *115*, 7729; c)A. K. Inge, X. D. Zou, *Nanoporous Materials: Synthesis and Applications*, Taylor & Francis Group, London **2013.**
[4] a) C. T. Kresge, M. E. Leonowicz, W. J. Roth, J. C. Vartuli, J. S. Beck, *Nature* **1992**, *359*, 710; b) S. H. Joo, S. J. Choi, I. Oh, J. Kwak, Z. Liu, O. Terasaki, R. Ryoo, *Nature* **2001**, *412*, 169.
[5] a) H. Li, M. Eddaoudi, M. O'Keeffe, O. M. Yaghi, *Nature* **1999**, *402*, 276; b) N. L. Rosi, J. Eckert, M. Eddaoudi, D. T. Vodak, J. Kim, M. O'Keeffe, O. M. Yaghi, *Science* **2003**, *300*, 1127; c) A. Phan, C. J. Doonan, F. J. Uribe-Romo, C. B. Knobler, M. O'Keeffe, O. M. Yaghi, *Acc. Chem. Res.* **2009**, *43*, 58.
[6] a) F. J. Uribe-Romo, J. R. Hunt, H. Furukawa, C. Klöck, M. O'Keeffe, O. M. Yaghi, *J. Am. Chem. Soc.* **2009**, *131*, 4570; b) A. P. Côté, A. I. Benin, N. W. Ockwig, M. O'Keeffe, A. J. Matzger, O. M. Yaghi, *Science* **2005**, *310*, 1166; c) H. M. El-Kaderi, J. R. Hunt,

J. L. Mendoza-Cortés, A. P. Côté, R. E. Taylor, M. O'Keeffe, O. M. Yaghi, *Science* **2007**, *316*, 268.
[7] a) A. K. Inge, M. V. Peskov, J. Sun, X. D. Zou, *Cryst. Growth Des.* **2011**, *12*, 369; b) X. D. Zou, T. Conradsson, M. Klingstedt, M. S. Dadachov, M. O'Keeffe, *Nature* **2005**, *437*, 716.
[8] J. Su, Y. Wang, Z. Wang, J. Lin, *J. Am. Chem. Soc.* **2009**, *131*, 6080.
[9] L. Tang, L. Shi, C. Bonneau, J. Sun, H. Yue, A. Ojuva, B.-L. Lee, M. Kritikos, R. G. Bell, Z. Bacsik, J. Mink, X. D. Zou, *Nature Mater.* **2008**, *7*, 381.
[10] Y. Xu, Y. Li, Y. Han, X. Song, J. Yu, *Angew. Chem. Int. Ed.* **2013**, *52*, 5501.
[11] Y. Han, Y. Li, J. Yu, R. Xu, *Angew. Chem. Int. Ed.* **2011**, *50*, 3003.
[12] a) X. Song, Y. Li, L. Gan, Z. Wang, J. Yu, R. Xu, *Angew. Chem. Int. Ed.* **2009**, *48*, 314; b) L. Shao, Y. Li, J. Yu, R. Xu, *Inorg. Chem.* **2011**, *51*, 225; c) Z. Liu, X. Song, J. Li, Y. Li, J. Yu, R. Xu, *Inorg. Chem.* **2012**, *51*, 1969.
[13] J. A. Armstrong, M. T. Weller, *J. Am. Chem. Soc.* **2010**, *132*, 15679.
[14] C. Baerlocher, T. Weber, L. B. McCusker, L. Palatinus, S. I. Zones, *Science* **2011**, *333*, 1134.
[15] a) R. W. Grosse-Kunstleve, L. B. McCusker, C. Baerlocher, *J. Appl. Crystallogr.* **1997**, *30*, 985; b) A. Altomare, M. C. Burla, M. Camalli, B. Carrozzini, G. L. Cascarano, C. Giacovazzo, A. Guagliardi, A. G. G. Moliterni, G. Polidori, R. Rizzi, *J. Appl. Crystallogr.* **1999**, *32*, 339; c) C. Baerlocher, L. B. McCusker, L. Palatinus, *Z. Kristallogr.* **2007**, *222*, 47.
[16] a) A. Cantín, A. Corma, S. Leiva, F. Rey, J. Rius, S. Valencia, *J. Am. Chem. Soc.* **2005**, *127*, 11560; b) A. Corma, M. J. Diaz-Cabanas, J. L. Jorda, C. Martinez, M. Moliner, *Nature* **2006**, *443*, 842; c) A. Corma, M. J. Diaz-Cabanas, J. L. Jorda, F. Rey, G. Sastre, K. G. Strohmaier, *J. Am. Chem. Soc.* **2008**, *130*, 16482; d) J. Jiang, J. L. Jorda, M. J. Diaz-Cabanas, J. Yu, A. Corma, *Angew. Chem. Int. Ed.* **2010**, *49*, 4986; e) M. Hernández-Rodríguez, J. L. Jordá, F. Rey, A. Corma, *J. Am. Chem. Soc.* **2012**, *134*, 13232.
[17] a) D. Xie, L. B. McCusker, C. Baerlocher, *J. Am. Chem. Soc.* **2011**, *133*, 20604; b) S. Elomari, A. W. Burton, K. Ong, A. R. Pradhan, I. Y. Chan, *Chem. Mater.* **2007**, *19*, 5485; c) L. B. McCusker, C. Baerlocher, A. W. Burton, S. I. Zones, *Solid State Sciences* **2011**, *13*, 800; d) D. Xie, L. B. McCusker, C. Baerlocher, S. I. Zones, W. Wan, X. D. Zou, *J. Am. Chem. Soc.* **2013**, *135*, 10519; e) S. Elomari, A. Burton, R. C. Medrud, R. Grosse-Kunstleve, *Micropor. Mesopor. Mater.* **2009**, *118*, 325.
[18] a) Y. Lorgouilloux, M. Dodin, J.-L. Paillaud, P. Caullet, L. Michelin, L. Josien, O. Ersen, N. Bats, *J. Solid State Chem.* **2009**, *182*, 622; b) M. Dodin, J.-L. Paillaud, Y. Lorgouilloux, P. Caullet, E. Elkaïm, N. Bats, *J. Am. Chem. Soc.* **2010**, *132*, 10221.
[19] L. B. McCusker, C. Baerlocher, S. T. Wilson, R. W. Broach, *J. Phys. Chem. C* **2009**, *113*, 9838.
[20] Z. Han, A. L. Picone, A. M. Z. Slawin, V. R. Seymour, S. E. Ashbrook, W. Zhou, S. P. Thompson, J. E. Parker, P. A. Wright, *Chem. Mater.* **2010**, *22*, 338.
[21] a) D. L. Dorset, G. J. Kennedy, *J. Phys. Chem. B* **2005**, *109*, 13891; b) D. Xie, L. B. McCusker, C. Baerlocher, L. Gibson, A. W. Burton, S.-J. Hwang, *J. Phys. Chem. C* **2009**, *113*, 9845.
[22] R. W. Broach, R. M. Kirchner, *Micropor. Mesopor. Mater.* **2011**, *143*, 398.
[23] E. Verheyen, L. Joos, K. Van Havenbergh, E. Breynaert, N. Kasian, E. Gobechiya, K. Houthoofd, C. Martineau, M. Hinterstein, F. Taulelle, V. Van Speybroeck, M. Waroquier, S. Bals, G. Van Tendeloo, C. E. A. Kirschhock, J. A. Martens, *Nature Mater.* **2012**, *11*, 1059.
[24] S. J. Sedlmaier, M. Döblinger, O. Oeckler, J. Weber, J. Schmedt auf der Günne, W. Schnick, *J. Am. Chem. Soc.* **2011**, *133*, 12069.
[25] A. K. Inge, H. Fahlquist, T. Willhammar, Y. N. Huang, L. B. McCusker, X. D. Zou, *J. Appl. Crystallogr.* **2013**, *46*, 1094.
[26] F. Gramm, C. Baerlocher, L. B. McCusker, S. J. Warrender, P. A. Wright, B. Han, S. B. Hong, Z. Liu, T. Ohsuna, O. Terasaki, *Nature* **2006**, *444*, 79.
[27] C. Baerlocher, F. Gramm, L. Massuger, L. B. McCusker, Z. B. He, S. Hovmöller, X. D. Zou, *Science* **2007**, *315*, 1113.
[28] C. Baerlocher, D. Xie, L. B. McCusker, S. J. Hwang, I. Y. Chan, K. Ong, A. W. Burton, S. I. Zones, *Nature Mater.* **2008**, *7*, 631.
[29] D. L. Dorset, K. G. Strohmaier, C. E. Kliewer, A. Corma, M. J. Díaz-Cabañas, F. Rey, C. J. Gilmore, *Chem. Mater.* **2008**, *20*, 5325.
[30] J. L. Sun, C. Bonneau, A. Cantin, A. Corma, M. J. Diaz-Cabanas, M. Moliner, D. L. Zhang, M. R. Li, X. D. Zou, *Nature* **2009**, *458*, 1154.
[31] M. Moliner, T. Willhammar, W. Wan, J. Gonzalez, F. Rey, J. L. Jorda, X. D. Zou, A. Corma, *J. Am. Chem. Soc.* **2012**, *134*, 6473.
[32] T. Willhammar, J. L. Sun, W. Wan, P. Oleynikov, D. L. Zhang, X. D. Zou, M. Moliner, J. Gonzalez, C. Martinez, F. Rey, A. Corma, *Nature Chem.* **2012**, *4*, 188.
[33] A. Corma, M. J. Díaz-Cabañas, J. Jiang, M. Afeworki, D. L. Dorset, S. L. Soled, K. G. Strohmaier, *Proc. Natl. Acad. Sci. USA* **2010**, *107*, 13997.
[34] J. Jiang, J. L. Jorda, J. Yu, L. A. Baumes, E. Mugnaioli, M. J. Diaz-Cabanas, U. Kolb, A. Corma, *Science* **2011**, *333*, 1131.
[35] R. Martínez-Franco, M. Moliner, Y. F. Yun, J. L. Sun, W. Wan, X. D. Zou, A. Corma, *Proc. Natl. Acad. Sci. USA* **2013**, *110*, 3749.
[36] Z. B. Yu, Y. Han, L. Zhao, S. L. Huang, Q. Y. Zheng, S. Z. Lin, A. Cordova, X. D. Zou, J. L. Sun, *Chem. Mater.* **2012**, *24*, 3701.
[37] a) M. Pan, *Micron* **1996**, *27*, 219; b) I. Diaz, A. Mayoral, *Micron* **2011**, *42*, 512; c) M. W. Anderson, T. Ohsuna, Y. Sakamoto, Z. Liu, A. Carlsson, O. Terasaki, *Chem. Commun.* **2004**, *0*, 907; d) J. L. Sun, X. D. Zou, *Dalton Trans.* **2010**, *39*, 8355; e) Z. Liu, N. Fujita, K. Miyasaka, L. Han, S. M. Stevens, M. Suga, S. Asahina, B. Slater, C. Xiao, Y. Sakamoto, M. W. Anderson, R. Ryoo, O. Terasaki, *Microscopy* **2013**, *62*, 109.
[38] R. Vincent, P. A. Midgley, *Ultramicroscopy* **1994**, *53*, 271.
[39] a) U. Kolb, T. Gorelik, C. Kübel, M. T. Otten, D. Hubert, *Ultramicroscopy* **2007**, *107*, 507; b) U. Kolb, T. Gorelik, M. T. Otten, *Ultramicroscopy* **2008**, *108*, 763.
[40] a) D. L. Zhang, P. Oleynikov, S. Hovmöller, X. D. Zou, *Z. Kristallogr.* **2010**, *225*, 94; b) W. Wan, J. L. Sun, J. Su, S. Hovmöller, X. D. Zou, *J. Appl. Crystallogr.* **2013**, *46*, 1863; c) W. Wan, J. L. Sun, S. Hovmöller, X. D. Zou, http://www.calidris-em.com/, accessed: April, 2013.
[41] S. Hovmöller, *Ultramicroscopy* **1992**, *41*, 121.
[42] X. D. Zou, M. Sundberg, M. Larine, S. Hovmöller, *Ultramicroscopy* **1996**, *62*, 103.
[43] a) W. Wan, S. Hovmöller, X. D. Zou, *Ultramicroscopy* **2012**, *115*, 50; b) W. Wan, S. Hovmöller, X. D. Zou, QFocus: http://www.mmk.su.se/electron-crystallography, accessed: May **2012**.
[44] X. D. Zou, S. Hovmöller, P. Oleynikov, *Electron Crystallography – Electron Microscopy and Electron Diffraction*, Oxford University Press, Oxford, UK **2011**.
[45] B. K. Vaĭnshteĭn, *Structure Analysis by Electron Diffraction,* , Pergamon Press, Oxford, NY **1964**.
[46] X. D. Zou, Y. Sukharev, S. Hovmöller, *Ultramicroscopy* **1993**, *49*, 147.
[47] S. Nicolopoulos, J. M. Gonzalez-Calbet, M. Vallet-Regi, A. Corma, C. Corell, J. M. Guil, J. Perez-Pariente, *J. Am. Chem. Soc.* **1995**, *117*, 8947.
[48] T. E. Weirich, X. D. Zou, R. Ramlau, A. Simon, G. L. Cascarano, C. Giacovazzo, S. Hovmöller, *Acta Crystallogr. A* **2000**, *56*, 29.
[49] D. L. Zhang, D. Grüner, P. Oleynikov, W. Wan, S. Hovmöller, X. D. Zou, *Ultramicroscopy* **2010**, *111*, 47.
[50] P. Oleynikov, S. Hovmöller, X. D. Zou, *Ultramicroscopy* **2007**, *107*, 523.

[51] M. Gemmi, X. D. Zou, S. Hovmöller, A. Migliori, M. Vennström, Y. Andersson, *Acta Crystallogr.* **2003**, *A59*, 117.
[52] D. L. Dorset, C. J. Gilmore, J. L. Jorda, S. Nicolopoulos, *Ultramicroscopy* **2007**, *107*, 462.
[53] T. E. Weirich, R. Ramlau, A. Simon, S. Hovmöller, X. D. Zou, *Nature* **1996**, *382*, 144.
[54] X. D. Zou, Z. M. Mo, S. Hovmöller, X. Z. Li, K. H. Kuo, *Acta Crystallogr.* **2003**, *A59*, 526.
[55] P. Wagner, O. Terasaki, S. Ritsch, J. G. Nery, S. I. Zones, M. E. Davis, K. Hiraga, *J. Phys. Chem. B* **1999**, *103*, 8245.
[56] D. L. Dorset, *Z. Kristallogr.* **2006**, *221*, 260.
[57] a) C. J. Gilmore, W. Dong, D. L. Dorset, *Acta Crystallogr.* **2008**, *A64*, 284; b) C. J. Gilmore, W. Dong, D. L. Dorset, *Acta Crystallogr.* **2008**, *A64*, 295; c) D. L. Dorset, *Z. Kristallogr.* **2003**, *218*, 458; d) D. L. Dorset, *Z. Kristallogr.* **2003**, *218*, 525; e) D. L. Dorset, *Z. Kristallogr.* **2003**, *218*, 612.
[58] C. J. Gilmore, G. Bricogne, *Methods Enzymol.* **1977**, *277*, 65.
[59] R. W. Grosse-Kunstleve, L. B. McCusker, C. Baerlocher, *J. Appl. Crystallogr.* **1997**, *30*, 985.
[60] a) G. Oszlányi, A. Sütő, *Acta Crystallogr.* **2004**, *A60*, 134; b) G. Oszlányi, A. Sütő, *Acta Crystallogr.* **2005**, *A61*, 147.
[61] L. Palatinus, G. Chapuis, *J. Appl. Crystallogr.* **2007**, *40*, 786.
[62] D. Xie, C. Baerlocher, L. B. McCusker, *J. Appl. Crystallogr.* **2008**, *41*, 1115.
[63] C. Baerlocher, L. B. McCusker, L. Palatinus, *Z. Kristallogr.* **2007**, *222*, 47.
[64] a) E. Mugnaioli, U. Kolb, *Micropor. Mesopor. Mater.* **2013**, *166*, 93; b) J. Su, E. Kapaca, L. F. Liu, V. Georgieva, W. Wan, J. L. Sun, V. Valtchev, S. Hovmöller, X. D. Zou, *Micropor. Mesopor. Mater.* **2013**, DOI: 10.1016/j.micromeso.2013.10.014.
[65] G. M. Sheldrick, *Acta Crystallogr.* **2008**, *A64*, 112.
[66] M. C. Burla, R. Caliandro, M. Camalli, B. Carrozzini, G. L. Cascarano, C. Giacovazzo, M. Mallamo, A. Mazzone, G. Polidori, R. Spagna, *J. Appl. Crystallgr.* **2012**, *45*, 357.
[67] V. Petricek, M. Dusek, L. Palatinus, Jana 2006, The crystallographic computing system. Institute of Physics, Praha, Czech Republic, **2006**.
[68] a) J. M. Newsam, M. M. J. Treacy, W. T. Koetsier, C. B. Degruyter, *Proc. R. Soc. London, Ser. A* **1988**, *420*, 375; b) M. M. J. Treacy, J. M. Newsam, *Nature* **1988**, *332*, 249.
[69] J. B. Higgins, R. B. Lapierre, J. L. Schlenker, A. C. Rohrman, J. D. Wood, G. T. Kerr, W. J. Rohrbaugh, *Zeolites* **1988**, *8*, 446.
[70] a) R. F. Lobo, M. Pan, I. Chan, H. X. Li, R. C. Medrud, S. I. Zones, P. A. Crozier, M. E. Davis, *Science* **1993**, *262*, 1543; b) R. F. Lobo, M. Pan, I. Chan, R. C. Medrud, S. I. Zones, P. A. Crozier, M. E. Davis, *J. Phys. Chem.* **1994**, *98*, 12040.
[71] a) R. F. Lobo, M. Tsapatsis, C. C. Freyhardt, I. Chan, C. Y. Chen, S. I. Zones, M. E. Davis, *J. Am. Chem. Soc.* **1997**, *119*, 3732; b) H. van Koningsveld, R. F. Lobo, *J. Phys. Chem. B* **2003**, *107*, 10983.
[72] M. E. Leonowicz, J. A. Lawton, S. L. Lawton, M. K. Rubin, *Science* **1994**, *264*, 1910.
[73] J. F. Ruan, P. Wu, B. Slater, O. Terasaki, *Angew. Chem. Int. Ed.* **2005**, *44*, 6719.
[74] a) M. W. Anderson, O. Terasaki, T. Ohsuna, A. Philippou, S. P. Mackay, A. Ferreira, J. Rocha, S. Lidin, *Nature* **1994**, *367*, 347; b) M. W. Anderson, O. Terasaki, T. Ohsuna, P. J. O. Malley, A. Philippou, S. P. Mackay, A. Ferreira, J. Rocha, S. Lidin, *Philos. Mag. B* **1995**, *71*, 813.
[75] R. F. Lobo, M. Tsapatsis, C. C. Freyhardt, S. Khodabandeh, P. Wagner, C. Y. Chen, K. J. Balkus, S. I. Zones, M. E. Davis, *J. Am. Chem. Soc.* **1997**, *119*, 8474.
[76] A. Corma, M. J. Diaz-Cabanas, F. Rey, S. Nicolooulas, K. Boulahya, *Chem. Commun.* **2004**, 1356.
[77] T. Willhammar, X. D. Zou, *Z. Kristallogr.* **2013**, *228*, 11.
[78] J.-L. Paillaud, B. Harbuzaru, J. Patarin, N. Bats, *Science* **2004**, *304*, 990.
[79] X. D. Zou, A. Hovmöller, S. Hovmöller, *Ultramicroscopy* **2004**, *98*, 187.
[80] J. L. Sun, Z. B. He, S. Hovmöller, X. D. Zou, F. Gramm, C. Baerlocher, L. B. McCusker, *Z. Kristallogr.* **2010**, *225*, 77.
[81] A. W. Burton, S. Elomari, I. Chan, A. Pradhan, C. Kibby, *J. Phys. Chem. B* **2005**, *109*, 20266.
[82] Z. Liu, T. Ohsuna, O. Terasaki, M. A. Camblor, M. J. Diaz-Cabanas, K. Hiraga, *J. Am. Chem. Soc.* **2001**, *123*, 5370.
[83] T. Ohsuna, Z. Liu, O. Terasaki, K. Hiraga, M. A. Camblor, *J. Phys. Chem. B* **2002**, *106*, 5673.
[84] A. Corma, M. Moliner, A. Cantin, M. J. Diaz-Cabanas, J. L. Lorda, D. L. Zhang, J. L. Sun, K. Jansson, S. Hovmoller, X. D. Zou, *Chem. Mater.* **2008**, *20*, 3218.
[85] M. Moliner, J. Gonzalez, M. T. Portilla, T. Willhammar, F. Rey, F. J. Llopis, X. D. Zou, A. Corma, *J. Am. Chem. Soc.* **2011**, *133*, 9497.
[86] T. Conradsson, M. S. Dadachov, X. D. Zou, *Micropor. Mesopor. Mater.* **2000**, *41*, 183.
[87] D. Denysenko, M. Grzywa, M. Tonigold, B. Streppel, I. Krkljus, M. Hirscher, E. Mugnaioli, U. Kolb, J. Hanss, D. Volkmer, *Chem. Eur. J.* **2011**, *17*, 1837.
[88] M. Feyand, E. Mugnaioli, F. Vermoortele, B. Bueken, J. M. Dieterich, T. Reimer, U. Kolb, D. de Vos, N. Stock, *Angew. Chem. Int. Ed.* **2012**, *51*, 10373.
[89] a) X. Huang, J. Zhang, X. Chen, *Chin. Sci. Bull.* **2003**, *48*, 1531; b) K. S. Park, Z. Ni, A. P. Côté, J. Y. Choi, R. Huang, F. J. Uribe-Romo, H. K. Chae, M. O'Keeffe, O. M. Yaghi, *Proc. Natl. Acad. Sci. USA* **2006**, *103*, 10186.
[90] B. Xiao, P. J. Byrne, P. S. Wheatley, D. S. Wragg, X. B. Zhao, A. J. Fletcher, K. M. Thomas, L. Peters, J. S. O. Evans, J. E. Warren, W. Z. Zhou, R. E. Morris, *Nature Chem.* **2009**, *1*, 289.
[91] M. Hmadeh, Z. Lu, Z. Liu, F. Gándara, H. Furukawa, S. Wan, V. Augustyn, R. Chang, L. Liao, F. Zhou, E. Perre, V. Ozolins, K. Suenaga, X. Duan, B. Dunn, Y. Yamamto, O. Terasaki, O. M. Yaghi, *Chem. Mater.* **2012**, *24*, 3511.
[92] H. Deng, S. Grunder, K. E. Cordova, C. Valente, H. Furukawa, M. Hmadeh, F. Gándara, A. C. Whalley, Z. Liu, S. Asahina, H. Kazumori, M. O'Keeffe, O. Terasaki, J. F. Stoddart, O. M. Yaghi, *Science* **2012**, *336*, 1018.
[93] C. T. Kresge, M. E. Leonowicz, W. J. Roth, J. C. Vartuli, J. S. Beck, *Nature* **1992**, *359*, 710.
[94] T. Yanagisawa, T. Shimizu, K. Kuroda, C. Kato, *Bull. Chem. Soc. Jpn.* **1990**, *63*, 988.
[95] A. Carlsson, M. Kaneda, Y. Sakamoto, O. Terasaki, R. Ryoo, S. H. Joo, *J. Electron Microsc.* **1999**, *48*, 795.
[96] Y. Sakamoto, M. Kaneda, O. Terasaki, D. Y. Zhao, J. M. Kim, G. Stucky, H. J. Shim, R. Ryoo, *Nature* **2000**, *408*, 449.
[97] C. B. Gao, Y. Sakamoto, K. Sakamoto, O. Terasaki, S. N. Che, *Angew. Chem. Int. Ed.* **2006**, *45*, 4295.
[98] T. Yu, H. Zhang, X. W. Yan, Z. X. Chen, X. D. Zou, P. Oleynikov, D. Y. Zhao, *J. Phys. Chem. B* **2006**, *110*, 21467.
[99] a) Y. Han, D. L. Zhang, L. L. Chng, J. L. Sun, L. Zhao, X. D. Zou, J. Y. Ying, *Nature Chem.* **2009**, *1*, 123; b) D. L. Zhang, J. L. Sun, Y. Han, X. D. Zou, *Micropor. Mesopor. Mater.* **2011**, *146*, 88.
[100] Y. F. Zhao, D. L. Zhang, L. Zhao, G. C. Wang, Y. H. Zhu, A. Cairns, J. L. Sun, X. D. Zou, Y. Han, *Chem. Mater.* **2011**, *23*, 3775.